Revision 2

Crystallization and melt extraction of a garnet-bearing charnockite from South China: Constraints from petrography, geochemistry, mineral thermometer and rhyolite-MELTS modeling

Xi-Song Zhang, Xi-Sheng Xu*, Yan Xia, Kai Zhao

***Corresponding Author**: Xi-Sheng Xu

Xi-Song Zhang: State Key Laboratory for Mineral Deposits Research, School of Earth Sciences and Engineering, Nanjing University, Nanjing, 210023, China;
Email: xisongzhang6@126.com

Xi-Sheng Xu: State Key Laboratory for Mineral Deposits Research, School of Earth Sciences and Engineering, Nanjing University, Nanjing, 210023, China;
Email: xsxu@nju.edu.cn

Yan Xia: State Key Laboratory for Mineral Deposits Research, School of Earth Sciences and Engineering, Nanjing University, Nanjing, 210023, China;
Email: xiayan@nju.edu.cn

Kai Zhao: State Key Laboratory for Mineral Deposits Research, School of Earth Sciences and Engineering, Nanjing University, Nanjing, 210023, China;
Email: kaivino920@hotmail.com

This is the peer-reviewed, final accepted version for American Mineralogist, published by the Mineralogical Society of America.
The published version is subject to change. Cite as Authors (Year) Title. American Mineralogist, in press.
DOI: https://doi.org/10.2138/am-2020-7335. http://www.minsocam.org/

Crystallization and melt extraction of a garnet-bearing charnockite from South China: Constraints from petrography, geochemistry, mineral thermometer and rhyolite-MELTS modeling

Xi-Song Zhang, Xi-Sheng Xu*, Yan Xia, Kai Zhao

State Key Laboratory for Mineral Deposits Research, School of Earth Sciences and Engineering, Nanjing University, Nanjing, 210023, China

Abstract

It is common for granitic rocks in high-grade terranes to undergo amphibolite-granulite facies metamorphic overprint, thus recovering magmatic records from the metamorphic modification remains a major challenge. Here, we report an early Paleozoic, garnet-bearing Yunlu charnockite, which outcropped in the Yunkai terrane of the Cathaysia block from South China, and underwent amphibole-grade metamorphic overprint in the late Devonian. Field observation, micro-texture and mineral geochemistry combining with diffusion modeling constrain that the metamorphic overprint with extremely short-duration of ~0.2-0.5 Ma only influences a narrow rim of < 100 μm for most minerals. The magmatic information is able to be retrieved combining with rhyolite-MELTS modeling, mineral thermobarometry using mineral core compositions to quantitatively estimate magmatic pressure, temperature and melt H_2O contents. Rhyolite-MELTS modeling results are evaluated by comparison with experimentally-determined phase relations for a peraluminous granite with ~69.83 wt.% SiO_2 at a pressure of ~500 MPa. The comparison results suggest that the modeling reproduces phase relationships of feldspars and quartz within 20-60 °C below 7.0 wt% melt H_2O, but fails to work properly for all phases at melt H_2O contents higher than 7.0 wt%. The modeling results using reconstructed primary magma composition of the Yunlu charnockite combining with the orthopyroxene-garnet-plagioclase-quartz thermobarometry and fluid inclusion analyses suggest that the magma was emplaced at pressure of ~600 MPa, temperature of >900 °C, and initial H_2O content

of ~4.0 wt% with rare CO_2 components. The orthopyroxene-garnet, biotite-garnet, and biotite-orthopyroxene thermometers yield a consistent temperature range of 770-820 ± 60 °C, which is significantly higher than the H_2O-saturated solidus temperature of ~630 °C estimated from experimental results and two-feldspar thermometry. This suggests that the early crystallized minerals (e.g. garnet, orthopyroxene and some euhedral biotite) of the Yunlu charnockite equilibrate at higher temperature with crystallinities of ~30-45 %, rather than the H_2O-saturated solidus conditions. We thus propose a hypothesis of melt extraction at 780-820 °C in a deep-seated, slowly cooling, partially crystalline magma reservoir. The melt extraction physically segregates the early crystallized minerals from residual interstitial melts, which inhibits element diffusion equilibration between these minerals and interstitial melts. Granite thermometry commonly yields large range of temperature estimations, which may be related to melt extraction events. Our study shows that melt extraction recorded in granites can be identified by combining micro-texture, mineral thermometry and rhyolite-MELTS modeling, which further provides quantitative insights for fractionation process of silicic magmas.

Keywords: garnet-bearing charnockite, rhyolite-MELTS modeling, mineral thermometer, melt extraction, metamorphic overprint

1. Introduction

Orthopyroxene-bearing granitoid (charnockite), although rarely outcropped, represents one of important constituents of the middle-lower continental crust, which provides critical information on formation and differentiation of the continental crust (Frost and Frost 2008; Le Maitre, 2002; Rajesh and Santosh 2012). Charnockite by definition can be igneous rock, i.e. solidified magma at low H_2O activity and elevated solidus temperature within stability field of orthopyroxene (Frost et al., 2000; Harlov et al., 2013), or metamorphic rock, which experienced dehydration reaction to form orthopyroxene due to influx of low H_2O-activity fluids (Harlov et al., 2014; Newton et al., 2014; Yang et al., 2014). It remains a challenge to distinguish whether the orthopyroxene in the charnockite crystallized from magmas, or formed during a later high-grade metamorphic overprint (e.g. Rajesh et

al., 2011). This issue is even more prominent for Precambrian igneous charnockites, which is commonly subjected to later high-grade metamorphic overprint (Wang et al., 2018; Ma et al., 2013; Zhao et al., 2014; Mikhalsky and Kamenev., 2013). It is thus essential to distinguish the blending information of magmatism and metamorphism to understand the formation of charnockite, yet few attempts have been made to evaluate to what extent the metamorphic overprint has influenced the textures and compositions of the original igneous charnockites.

Melt extraction in silicic magma chambers has been considered to be responsible for the generation of crystal-poor rhyolites and high-SiO_2 granites (Bachmann and Bergantz 2004; Lee and Morton, 2015; Cashman et al. 2017). Compared to volcanic rocks, intrusive rocks retain a more integrated record of the magma chamber dynamics (Fiedrich et al. 2017). Thus, seeking the evidence related to crystal accumulation and melt extraction in silicic intrusive rocks is urgent and gains more and more attention (e.g., Friedrich et al. 2017; Hartung et al. 2017; Schaen et al. 2018; Zhao et al. 2018). Recent studies have claimed that peraluminous charnockite may crystallize without involvement of low H_2O-activity fluids and represent granitic cumulate after extraction of evolved interstitial melt through compaction of the crystal framework in a mush reservoir (Zhao et al. 2017, 2018). Such petrogenetic model is different from that for the metaluminous charnockite for which melt extraction is not necessary to be invoked if low H_2O-activity fluids have significantly elevated the solidus temperature within stability field of orthopyroxene (Frost et al., 1999, 2000; Harlov et al., 2013). Peraluminous charnockite is seldom reported so far, except for the Triassic, cordierite-bearing charnockite from Jiuzhou in South China (Zhao et al. 2017, 2018) and the Cenozoic, garnet-orthopyroxene tonalite in Niikappu River area from Hidaka Metamorphic Belt, northern Japan (Shimura et al. 1992, 2004). Hence, the rarely outcrop of the peraluminous charnockite severely restricts our understanding not only of the magmatic fluid conditions and crystallization processes of the igneous charnockite, but also the silicic magma differentiation mechanism in the continental crust.

Constraining the intensive parameters (e.g. pressure, temperature and oxygen fugacity) that characterize the emplacement and crystallization of granitic rocks remains challenging. (Anderson 1996, 2008; Bartoli et al. 2014; Zhao et al. 2017). Experimentally- and empirically-calibrated thermobarometers afford the most convenient approach for estimating magmatic crystallization temperatures (Anderson et al. 2008; Putirka 2008). In theory, major element-based mineral-pair thermometers in intrusive rocks should yield consistent near-solidus temperatures only if: (1) the magma crystallizes under conditions of low undercooling or low cooling rate and (2) various mineral crystals and co-existed melt keep in continuously chemical equilibrium. This is true for some cases (Frost et al. 2000; Harlov et al. 2013; Zhang et al. 2006), but not for cases where a large range of temperatures are retrieved from the various mineral thermometers (Elliott et al. 1998; Moazzen and Droop 2005; Shimura et al. 1992; Wang et al. 2018). The latter may indicate that the mineral compositions do not represent equilibrium compositions at near-solidus temperatures due to one or more of: 1) various degrees of crystal-melt disequilibrium for the crystallized mineral assemblages (Best 2003); 2) resetting of mineral compositions by later thermal events (metamorphic overprint, Saha et al. 2008; Bhowmik et al. 2009); 3) high-temperature magma recharge (Pietranik et al. 2006; Wiebe et al. 2007), and/or other processes (e.g., crystal entrainment during ascent, Anderson 2008). These factors are fundamental issues in granite thermometry, but have not been fully assessed so far.

As one of the few peraluminous, igneous charnockite around the world, the Yunlu garnet-bearing charnockite contains diverse mineral assemblages and textures associated with crystal-melt reactions and abundant symplectite/corona textures related to sub-solidus reactions, providing a rare opportunity to retrieve the micro-texture and pressure-temperature information at the magmatic and metamorphic stages of formation, respectively. We thus study here the whole-rock and mineral geochemistry, petrography, fluid inclusions, mineral thermobarometry and rhyolite-MELTS modeling of the Yunlu charnockite, aiming to distinguish the micro-textures and mineral assemblages associated with the magmatic and metamorphic stages of formation, and to quantitatively constrain

pressure and temperature conditions, reconstruct in detailed the crystallization processes, and decipher the enigmatic connections between mineral thermometry and magmatic crystallization processes.

2. Geological setting and field investigation

The early Paleozoic orogen in the SCB (South China Block) represents the first important crustal reworking event in the Phanerozoic (Li et al. 2010). It resulted in the remobilization of crystalline basement in the entire Cathaysia Block and the eastern Yangtze Block, and formed an orogenic belt stretching for ca. 2000 km in a northeasterly direction (Li et al. 2010; Wang et al. 2007). The orogeny caused an angular unconformity between pre-Devonian deformed strata and undeformed Devonian strata (Grabau 1924). Simultaneously, the early Paleozoic orogeny yielded voluminous syn-orogenic and post-orogenic granitoids and rare mafic rocks (Wang et al. 2013a, b; Yao et al. 2012; Zhang et al. 2015). The high-grade metamorphic rocks, which reach amphibolite- to granulite-facies grades, mainly occur in the northeastern Wuyi terrane and in the southwestern Yunkai terrane (Li et al. 2011; Wang et al. 2012; Yu et al. 2003, 2005, 2007, 2014).

Specifically, the early Paleozoic gneisses and gneissic migmatites underwent amphibolite- to granulite-facies metamorphism and local crustal anatexis and are regarded as part of the basement rocks in the Yunkai terrane (Wang et al. 2007). These basement rocks are mainly exposed in the Gaozhou area and are thus referred to as the Gaozhou Complex (Fig. 1a), which mainly consists of paragneiss, orthogneiss, gneissic migmatite/granite and charnockite. The charnockite is located near Yunlu village and named as the Yunlu garnet-bearing charnockite. It intrudes the gneissic migmatite/granite, as a lenticular body with an area of ~11 km^2 (Fig. 1b; Wang et al. 2013c). U-Pb dating of zircon and mineral thermometry constrain an early Paleozoic (~440 Ma), amphibole- to granulite-facies metamorphic event for the surrounding gneissic migmatite/granite (Wang et al. 2013c). Geochronological studies of this garnet-bearing charnockite have yielded an early Paleozoic emplacement age of ~440 Ma (Chen et al. 2012; Wang et al. 2013c). Because of thick vegetation and

poor outcrops, it is not easy to define the contact relationships between the garnet-bearing charnockite and surrounding gneissic migmatite/granite. Different kinds of xenolith are distinguished in the Yunlu garnet-bearing charnockite, notably of gneissic granite and garnet-biotite gneiss (Fig. 2a-b). The gneissic granite xenolith indicates that the Yunlu charnockite postdates the gneissic migmatite/granite.

3 Petrography, mineral chemistry and fluid inclusion

3.1 Petrography and mineral chemistry

The Yunlu garnet-bearing charnockite has an unfoliated, massive structure (Fig. 2a). It contains orthopyroxene, garnet, biotite, ilmenite, K-feldspar, plagioclase, quartz and minor accessory minerals (apatite, monazite, pyrrhotite, and zircon). Details about the mineral shape, size, inclusion, occurrence and composition are listed on Table 1. The major element compositions of the rock-forming minerals are listed in Appendix Table 1. The trace element compositions of garnet and orthopyroxene measured by LA-ICP-MS are listed in Appendix Table 2. Details of the analytical methods are described in the supplementary material.

3.1.1 Garnet

The garnet crystals are presented as three groups: group 1 garnet (Grt_1) consists of large (1-6 mm), euhedral crystals with a few mineral inclusions (Qz, Ilm) and regular grain boundaries, while group 2 garnet (Grt_2) consists of subhedral to anhedral crystals (1-3 mm) with irregular grain boundary outlines against partial or complete rim of biotite and quartz intergrowths (Fig. 2e). The group 3 garnet (Grt_3) consists of small (10-100 μm), globular, anhedral crystals distributed along plagioclase-ilmenite/orthopyroxene/biotite grain boundaries (Fig. 3). Regarding major element compositions, all groups of garnet crystals (Grt_1, Grt_2, Grt_3) have similar FeO contents, showing these garnets are almandites (Alm = 64-69; Table 1). Both Grt_1 and Grt_2 crystal exhibit Ca-rich and Mg-poor rims (Grt_1 & Grt_2 rim, ~ 50 μm) (Fig. 4c, e, f). Grt_3 crystals exhibit lower MgO and higher

CaO contents than Grt_1 and Grt_2 crystals, comparable to the Grt_1 & Grt_2 rim. Regarding trace element compositions, all groups of garnets have high contents of compatible elements such as Cr (104-174 ppm), V (141-161 ppm), Sc (139-201ppm) and Y (555-666 ppm). Flat to HREE-enriched patterns with clear negative Eu anomalies characterize Grt_1 crystals (Fig. 4d). The Grt_1 crystals have HREE and Y concentrations that decrease from core to rim (Fig. 4b). The Grt_3 crystals exhibit varying degrees of LREE-enrichment and HREE-depletion depending on the reactive minerals involved (Fig. 4d). Note also that the garnet crystals in Bt-Grt gneiss have high contents of MnO (6.03-6.56 wt%) and low contents of CaO (0.56-0.62 wt%) characteristics that are obviously different from Grt_1 and Grt_2 crystals in host garnet-bearing charnockite (Fig. 4e).

3.1.2 Orthopyroxene

The orthopyroxene crystals are 0.5-6 mm across (Fig. 2c-d), and can be divided into two groups based on their grain shapes and occurrences (Table 1). Group 1 orthopyroxenes (Opx_1) have euhedral shapes with regular grain boundaries. Group 2 orthopyroxenes (Opx_2) have subhedral to anhedral shapes with irregular grain boundaries against the partial or complete rims of biotite and quartz intergrowths (Fig. 2c). Both groups rarely contain mineral inclusions of plagioclase, ilmenite, biotite, and quartz. Opx_1 and Opx_2 exhibit indistinguishable compositional characteristics (Fig. 5a) except few grain rims (Opx_1 & Opx_2 rim) adjacent to the Grt_3, which show higher FeO and lower MgO contents. Both Opx_1 and Opx_2 have high FeO (29.63-35.10 wt%), low MgO (14.23-16.97 wt%), and extremely low CaO (0.04-0.46 wt%) contents, and so classify as ferro-hypersthene or ferrosilite (Fs = 49.4-56.0). In particular, no compositional zoning is observed within individual crystals. Both groups are enriched in compatible trace elements, e.g., Zn (616-655 ppm), Cr (147-285 ppm), V (260-515 ppm) and Sc (101-133 ppm). The chondrite-normalized REE patterns of orthopyroxenes are characterized by enrichment in MREE with strong negative Eu anomalies (Fig. 5b).

3.1.3 Biotite

The biotites can be separated into two groups based on crystal shapes and occurrences (Table 1).

Group 1 biotite (Bt_1) comprises euhedral, inclusion-free crystals, with a size range of 0.4-5 mm (Fig.2d). Group 2 biotite (Bt_2) crystals (0.5-2 mm) are subhedral to anhedral and form intergrowths with quartz that replace garnet/orthopyroxene crystals (Fig. 2c). Besides, the biotite crystals from the gneissic granite xenolith and the Grt-Bt gneiss xenolith were analyzed by EMP for comparison. On major element compositions, the biotite from the Yunlu charnockite shows higher TiO_2 contents (4.10-5.78 wt%) than Grt-Bt gneiss xenolith (0.07-0.21 wt%) and higher FeO contents (18.74-22.79 wt%) than gneissic granite xenolith (15.94-16.69 wt%) (Table 1). For the garnet-bearing charnockite, both groups of biotites (Bt_1 and Bt_2) have similar TiO_2 contents and X_{Mg} values irrespective of occurrence (Fig. 5d). They also have high contents of FeO (18.74-22.79 wt%) and thus classify as Fe-rich biotite.

3.1.4 Plagioclase

Plagioclase crystals are euhedral to subhedral with a size range of 0.5-3 mm (Fig. 2f). Some plagioclase crystals occur as mineral inclusions within orthopyroxene, with sizes of 0.1-0.3 mm (Fig. 2d). Based on their occurrences and compositions, the plagioclase crystals may be divided into two types (Table 1). Group 1 plagioclase (Pl_1) represents the large grain size with normal An zoning (36 mol% $\leq$ An $\leq$ 47 mol%, Fig. 5e). Group 2 plagioclase (Pl_2) represents plagioclase rim adjacent to Grt_3 crystals, which have the lowest An contents (An < 36 mol%). The histogram of An contents in Pl_1 shows a unimodal distribution with a peak at ca. An_{40}–An_{47}, with decreasing An contents towards the rims (Fig. 5f).

3.1.5 K-feldspar

The K-feldspar crystals show two groups (Table 1), group 1 K-feldspar (Kfs_1) exhibits euhedral shape with a size of 0.5-30 mm (Fig. 2a, f), while group 2 K-feldspar (Kfs_2) exhibits small globular grains (10-30 μm) distributed along the boundaries between biotite and plagioclase crystals (Fig. 3b). The big Kfs_1 crystals with grain size > 10 mm have orthoclase content of 82.9-86.9 mol% in their cores. In comparison, the Kfs_2 crystals have higher orthoclase contents, varying from 91.3-93.5

This is the peer-reviewed, final accepted version for American Mineralogist, published by the Mineralogical Society of America.
The published version is subject to change. Cite as Authors (Year) Title. American Mineralogist, in press.
DOI: https://doi.org/10.2138/am-2020-7335. http://www.minsocam.org/

mol%.

3.1.6 Ilmenite and quartz

The euhedral to subhedral ilmenite crystals are associated either with orthopyroxene and garnet or with mineral inclusions (0.1-0.2 mm) in orthopyroxene and garnet crystals (Fig. 2c, e). The quartz crystals can be separated into three groups based on their sizes and occurrences (Table 1). Group 1 quartz (Qz_1) displays euhedral to anhedral crystal shape and poikilitic texture with maximum diameters of 0.5-4 mm (Fig. 2d). Group 2 quartz (0.2-0.5 mm) (Qz_2) forms intergrowths with biotite replaced by orthopyroxene/garnet crystals (Fig. 2c). Group 3 quartz (~20-50 μm) (Qz_3) comprises symplectites on mineral grain boundaries (Fig. 3a-d).

3.2 Fluid inclusion

Fluid inclusions are not abundant in the Yunlu charnockite and are mostly found in quartz, and only rarely in orthopyroxene, garnet, biotite and feldspar. The fluid inclusions have emerged as single isolated individuals without cracks (Fig. 6a-b). They thus represent the most suitable candidates for primary fluid inclusions, i.e., inclusions that have formed during magmatic crystallization. Thirteen fluid inclusions were found in different groups of quartz crystals (six inclusions in Qz_1 and seven inclusions in Qz_2) are analyzed at room temperature. The fluid inclusions are mainly presented as H_2O-rich compositions irrespective of their occurrence (Qz_1 or Qz_2), apart from one inclusion from Qz_1 which is CO_2-H_2O-rich.

4. P-T estimations by thermo-barometers

The orthopyroxene–garnet–plagioclase–quartz barometer and the garnet–orthopyroxene thermometer are used here. The compositions of garnet in Yunlu charnockite are within the required garnet compositions (Appendix Table 1) with grossular contents of < 30 mol% and spessartine contents of < 5 mol% (Bhattacharya et al. 1991). The uncertainties of the barometer and thermometer are ~100 MPa and ~50 °C (Bhattacharya et al. 1991). Different authors have calibrated the biotite–

orthopyroxene thermometer (Aranovich et al. 1988; Sengupta et al. 1990; Wu et al. 1999). Here, we choose the thermometer from Wu et al. (1999), which provides the smallest uncertainty (± 60 °C). This thermometer is calibrated under amphibolite- to granulite-facies (590-860 °C) conditions and has been applied successfully in magmatic rocks (Zhao et al. 2017). The garnet-biotite thermometer with uncertainty of ~25 °C is used to constrain crystallization temperatures (Holdaway 2000, 2001) as in other granite bodies (Anderson 2008). The two-feldspar thermometer was calculated using the Solvcal 2.0 program of Wen and Nekvasil (1994) employing the activity models of Elkins and Grove (1990), Ghiorso (1984), and Fuhrman and Lindsley (1988). It is expected to yield reliable temperature estimations with an uncertainty of ~50 °C (Anderson 1996).

Detailed petrological and geochemical studies on ferromagnesian minerals in granitoids can provide insights into the physicochemical conditions of crystallization, such as pressure, temperature and melt-H_2O contents (Anderson 1996, 2008; Clemens and Wall 1988). The presence of almandine-rich garnet without cordierite in Yunlu charnockite indicates a relatively high emplacement pressure (Green 1976). For the Yunlu charnockite, the Grt_1 and Grt_2 (with average core grossular proportion of 4.7 mol%) coexist with Opx_1, Opx_2 with X_{Mg} values of 0.46, plagioclase (Pl_1 with average core An value of 46.2) and quartz (Qz_1) crystals, yielding an equilibrium pressure of 610 ± 100 MPa and a temperature of 820 ± 50 °C (Table 2). The euhedral biotite (Bt_1) with X_{Mg} values of 0.40 coexists with Opx_1, Opx_2 and Grt_1, Grt_2 crystals, which yield a temperature of 780 ± 60 °C and 770 ± 25 °C, respectively (Table 2). K-feldspar generally is the latest phase in peraluminous magma systems (Clemens and Birch 2012; Scaillet et al. 2016), thus it is inferred to co-crystallize with the rim of plagioclase. The two-feldspar thermometry using compositions of plagioclase rim (Pl_1 rim) and K-feldspar core (Kfs_1 core) yields a crystallization temperature of ~630 ± 50 °C. The small (10-100 μm), globular Grt_3 (with an average grossular value of 6.1 mol%) distributes along the grain boundaries between orthopyroxene/biotite/ilmenite and plagioclase (Pl_2

with average An value of 35.4). The compositions of Opx_1, Opx_2 rim combined with compositions of Grt_3, Pl_2 and Qz_3 yield pressure of 710 ± 100 MPa and temperature of 750 ± 50 °C (Table 2). The compositions of Bt_1, Bt_2 and the compositions of Grt_3 yield temperature of 720 ± 25 °C. The detailed temperatures and pressures obtained from various thermobarometers are listed on Table 2.

5. Rhyolite-MELTS modeling

Rhyolite-MELTS, a modified calibration of the original MELTS modeling, is designed to better capture the quartz and K-feldspar saturation surfaces which yields more accuracy in modeling silicic magmas (Gualda et al. 2012). It was mainly developed for metaluminous, silicic magma systems with crystallinities of < 50 % (Gualda et al. 2012), and has been widely applied to volcanic rocks at ≤ 200 MPa pressures (Bachmann et al. 2012; Gualda and Ghiorso 2013; Pamukcu et al. 2013). Although the uncertainties of this modeling have been evaluated by comparison with experimentally determined phase relationships (Gardner et al. 2014), these evaluations involved metaluminous compositions at ≤ 200 MPa pressure. The uncertainties remain unknown when applied to peraluminous, silicic magma systems at higher pressures (> 200 MPa). In this section, the rhyolite-MELTS modeling results (Gualda et al. 2012; Ghiorso and Gualda 2015) are first rigorously evaluated by comparison with the experimental data of a peraluminous system (Clemens and Birch 2012), then applied to the case of the Yunlu charnockite to simulate its geochemical variation and phase relationship.

5.1.1 Evaluation of uncertainties

A peraluminous, garnet-bearing ignimbrite (LMI 9399, Table 3), the starting material in Clemens and Birch's experiments, was chosen as the initial composition for modeling and the pressure was set at 500 MPa to facilitate the comparison. As shown in Fig. 7, the plagioclase and quartz saturated curves in the modeling are consistent with the experimentally determined curves with differences of < 60 °C irrespective of H_2O contents. For the K-feldspar, the modeling of the saturated curve matches the experimentally determined boundary within ~20 °C at low H_2O (< 6.0

296 wt%) contents, while the differences increase to 80 °C at high H_2O (~ 8.0 wt%) contents. The
297 modeled garnet curve is consistent with the experimentally determined curve with a difference of <
298 50 °C at > 5.5 wt% H_2O but is predicted at ~100 °C below the experimentally determined curve at
299 ~5.0 wt% H_2O. The modeling of the saturated curve of biotite is lower than the experimentally
300 determined curve with a difference of > 100 °C at both low and high H_2O contents. Similarity, the
301 modeled saturated curve of orthopyroxene-in is higher than the experimentally determined saturated
302 curve with a difference of > 100 °C. However, the orthopyroxene-out saturated curve, is predicted as
303 ~50 °C below the experimentally constrained curve irrespective of H_2O contents.

304 In summary, the rhyolite-MELTS modeling can predict phase relationships for quartz and two
305 feldspars within the acceptable differences of ~20-60 °C irrespective of H_2O contents, except for the
306 slightly larger difference of ~80 °C for K-feldspar at 8.0 wt% H_2O contents. Meanwhile, the
307 orthopyroxene-out saturated curve is well predicted by rhyolite-MELTS with the temperature
308 differences < 50 °C. The modeling results do, however, poorly constrain the phase relationships for
309 the garnet, biotite and orthopyroxene-in. The modeling results are consistent with the evaluation of
310 Gardner et al. (2014), who concluded that the rhyolite-MELTS could not always predict the saturated
311 curves of ferromagnesian minerals exactly. This may result from the deficiencies of thermodynamic
312 data of H_2O-rich silicate liquids and activity-composition models for ferromagnesian mineral phases
313 (i.e. pyroxene, garnet and biotite).

314 ### 5.1.2 Modeling the geochemical variation of the Yunlu charnockite

315 Whole rock compositions of the studied samples are generally used as input parameters of
316 system initial composition to constrain the phase relationship utilizing thermodynamic modeling.
317 This appears to be an over-simplification because the whole-rock composition may be modified by
318 various processes (e.g. Zhao et al., 2018). For the Yunlu charnockite, the major element compositions
319 are more mafic compared with the metasediment-derived experimental melts (Fig. 8), suggesting that
320 whole-rock compositions of charnockite samples have deviated from primary melt compositions.

The more mafic compositions of the Yunlu charnockite are likely caused by involvement of significant cumulate components (see below discussion), although mixing with more mafic magmas or entrainment of restitic materials may also have played minor roles as suggested by the homogeneous, enriched Nd-Hf isotopic compositions and the absence of restitic components (Wang et al. 2013; Qiu et al. 2018).

Here, we model the continuous compositional variation trend for the Yunlu charnockite based on an *in situ* (incremental) fractional crystallization process (Nishimura and Yanagi 2000; Hertogen and Mareels 2016; Zhao et al. 2018). In the modeling, the incremental fractionation with cumulate formation and melt extraction in a solidification front is considered by mass balance calculation (see details in supplementary material). Mass balance equations were solved by step-wise fashion in order to model such incremental fractionation. The interstitial melt composition in solidification front at each step is acquired by rhyolite-MELTS modeling, i.e. by determining the melt composition at the critical crystallinity of 40%. The geochemical modeling requires initial composition and H_2O contents as input parameters, while the former remains unknown and the latter are likely at a range of 2.0-5.0 wt% for typical peraluminous charnockites (Shimura et al. 1992; Zhao et al., 2017). We thus vary the initial compositions and H_2O contents to best fit the variation of the whole rock data. The initial H_2O contents of 2.0 wt% and 4.0 wt% are selected as representative. The most felsic charnockite sample D19-4 (with a SiO_2 content of 68.65 wt%, Table 3) is selected as a candidate because it has the most approximate composition with the metasediment-derived experimental melts (Fig. 8). The most mafic charnockite sample 15GZ19 with SiO_2 content of ~63.12 wt% may have experienced significant amount of melt loss, e.g. as high as 40% (Zhao et al. 2018, Appendix Table 3). The primary composition may be approximated through adding ~40% interstitial minimum melt into the whole-rock composition of sample 15GZ19. The interstitial minimum melt is the average chemical composition of Tilmunda granite in the New England batholith, which compositions are plotted very close to the minimum melting point on Q-An-Or ternary system (White and Chappell

346 1977, Appendix Table 5). We note that such method cannot precisely reconstruct the primary magma
347 composition, but at least provide a feasible way. Details of the model descriptions are provided in
348 supplementary material, while the results are given in Appendix Table 5 and summarized in Fig. 8.

349 The geochemical modeling results show that initial compositions and H_2O contents control the
350 modeled compositional trend. For instance, sample D19-4 has distinct higher CaO and lower Na_2O
351 contents compared to the sample MC01, which results in the obviously different modeled CaO and
352 K_2O content variations (Fig. 8). In addition, the modeled SiO_2 and MgO contents of sample D19-4
353 with 2.0 wt% initial H_2O content are significantly higher than sample D19-4 with 4.0 wt% H_2O. In
354 other words, the sample D19-4 with high H_2O content (4.0 wt%) define a better fitness to the Yunlu
355 charnockites compared to the same sample with low H_2O content (4.0 wt%). This comparison results
356 suggest that the Yunlu charnockite should contain higher H_2O contents. Compared with sample
357 D19-4, the virtual sample MC01 could better match the compositional variation of the Yunlu
358 charnockite although it shows slightly higher (by <0.5 wt%) modeled TiO_2 and slightly lower (by
359 <1.0 wt%) CaO contents than natural whole-rock contents (Fig. 8). The modeling result of MC01
360 predicts that the cumulate pile composition (cumulus solid plus unextracted melt) has ~63.30 wt% to
361 68.97 wt% SiO_2, which matches the range of the Yunlu whole-rock SiO_2 contents. Meanwhile, it also
362 best fits the compositional variation of FeO, MgO, Na_2O, and Al_2O_3 contents of the Yunlu
363 charnockite (Fig. 8).

364 ### 5.1.3 Modeling the phase relationship of the Yunlu charnockite

365 The thermodynamic modeling requires a series of input parameters, e.g. initial whole-rock
366 composition, fluid composition, pressure and temperature. Fractional crystallization modeling in
367 section 5.1.2 has shown the virtual composition MC01 is a suitable initial whole-rock composition
368 used for thermodynamic modeling. For the initial H_2O content, we use a range of H_2O contents from
369 2.0 wt% to 5.0 wt% with interval of 1.0 wt% in the modeling. The effect of CO_2 is also considered to
370 discuss its effects on mineral phase relationships and evolutional paths of mixed CO_2-H_2O fluids.

This is the peer-reviewed, final accepted version for American Mineralogist, published by the Mineralogical Society of America.
The published version is subject to change. Cite as Authors (Year) Title. American Mineralogist, in press.
DOI: https://doi.org/10.2138/am-2020-7335. http://www.minsocam.org/

Five different initial CO_2 contents (100, 500, 1000, 2000 and 3000 ppm) are employed in the modeling. The pressure is set at 600 MPa based on our barometric estimates. The crystallization temperature started at 1100 °C and ended at 630 °C, with an interval of 10 °C. Given that the Yunlu charnockite contains accessory ilmenite and pyrrhotite without magnetite, the oxygen fugacity is restricted to FMQ-1 (the fayalite–magnetite–quartz buffer assemblage) (Clemens and Birch 2012).

The modeling results are shown in Figs. 9, 10 and listed in Appendix Tables 6, 7. Results of the mixed H_2O-CO_2 fluid simulations show that the different initial CO_2 contents with fixed H_2O contents (4.0 wt%) have a substantial effect on the solidus temperature of the magma, e.g. ~820 °C with 0.3 wt% CO_2, ~720 °C with 0.2 wt% CO_2, and ~630 °C with 0.1 wt% CO_2. The exsolved fluid composition is CO_2-rich at 0.3 wt% CO_2 + 4.0 wt% H_2O conditions and contains 55 mol% CO_2 at near-solidus conditions. Under 0.2 wt% CO_2 + 4.0 wt% H_2O conditions, the fluids exsolved from the magma are gradually CO_2-poor and H_2O-rich, which contain 20 mol% CO_2 at near-solidus conditions. Under 0.1 wt% CO_2 + 4.0 wt% H_2O conditions, the fluid evolves to become more H_2O-rich as the system crystalizes, and the fluid eventually contains ~90 mol % H_2O at near H_2O-saturated solidus temperatures. The modeling results indicate that the granitic systems commonly evolve toward a CO_2-rich, H_2O-rich fluid composition at near-solidus temperatures when the magma contain $\leq$ 0.1 wt% initial CO_2 content.

At different initial melt H_2O contents without CO_2, orthopyroxene is always a liquidus phase, while the liquidus temperature is variable, i.e., it decreases from 1117 °C at 2.0 wt% initial H_2O, over 1097 °C and 1077 °C at 3.0 wt% and 4.0 wt% initial H_2O, to 1067 °C at 5.0 wt% initial H_2O (Fig. 10). Orthopyroxene disappears at ~777 °C at 2.0-5.0 wt% initial H_2O. The modeling predicts that garnet starts to crystallize at 857-887 °C at 2.0-5.0 wt% initial H_2O and down to H_2O-saturated solidus conditions at ~630 °C. The modeling predicts that biotite starts to saturate at 777 °C at 2.0-5.0 wt% initial H_2O (Fig. 10). Initial H_2O contents significantly influence the liqudus curves of quartz and plagioclase. Quartz and plagioclase saturation temperatures decrease from 927 °C and

977 °C at 2.0 wt% initial H_2O, over 877-837 °C and 927-877 °C at 3.0-4.0 wt% initial H_2O, to 817 °C at 5.0 wt% initial H_2O (Fig. 10). K-feldspar is predicted to crystallize at 807-737 °C at 2.0-5.0 wt% initial H_2O and thus it is the last phase to crystallize. Melt H_2O exhibits obviously incompatible characteristics during crystallization and it reach saturation at ~717 °C irrespective of H_2O contents (Fig. 10). The H_2O-saturated solidus is fixed at 630 °C using the experimental data of Clemens and Birch (2012) and Clemens and Phillips (2014).

6. Discussion

6.1 The Yunlu garnet-bearing charnockite: genetic type and metamorphic overprint

6.1.1 Igneous or metamorphic origin?

The charnockite could have either an igneous or a metamorphic origin depending on whether orthopyroxene crystallized directly from melt or formed by solid-state dehydration reaction during granulite-facies metamorphism (Frost and Frost 2008). The Yunlu charnockite lacks oriented structures such as foliation and lineation. No small (tens to hundreds of centimeters) irregular patches or veins of charnockite, which are the diagnostic characteristics of metamorphic charnockite, are found on the field outcrops (Newton et al. 2014). In addition, the xenoliths in the Yunlu charnockite were most likely captured when the host magma (charnockite) ascended and solidified (Fig. 2a). The reaction textures that group 2 biotite and quartz crystals (Bt_2 + Qz_2) surround, or the orthopyroxene (Opx_1 and Opx_2) and garnet (Grt_1 + Grt_2) crystals that they replace, indicate hydrous crystallization reaction during the magmatic stage (Fig. 2c-e) (Beard et al. 2004, 2005). The euhedral to subhedral, tabular plagioclase crystals form a skeleton texture, which is filled by anhedral, interstitial quartz crystals (Fig. 2f; Fig. S1b, d, f in supplementary material). The plagioclase crystals are characterized by normal anorthite zoning (Fig. 5e;). The plagioclase inclusions hosted in large plagioclase crystals (Fig. S1a, c, e in supplementary material) are typically euhedral in the Yunlu charnockite, retaining shapes that indicate growth in a melt-rich environment. Furthermore, the

420 $Grt_{1\&2}$, $Opx_{1\&2}$ and $Bt_{1\&2}$ porphyroblasts in granulites are euhedral to anhedral rather than rounded or
421 anhedral (Fig. 2d, e), and they share similar chemical compositions to those of igneous origin (see
422 below). All of the above favor an igneous origin for the Yunlu charnockite.

423 The Grt_1 and Grt_2 crystals have identical major element compositions and are classified as
424 almandite. They have low CaO and MnO contents, similar to those of the garnets from S-type
425 granitoids (Fig. 4e). Several pieces of petrographic and geochemical evidence indicate that the Grt_1
426 and Grt_2 crystals are of magmatic origin. (1) They exhibit euhedral shapes with few mineral
427 inclusions rather than the anhedral shapes (porphyroblast) or inclusion-rich peritectic or
428 metamorphic garnets from granulite and migmatite (Fig. 2e) (Acosta-Vigil et al. 2014; Dorais et al.
429 2009, 2012, 2014). (2) The compositional profiles of individual garnet grains reveal the near-flat
430 major element features from core to mantle, apart from a thin Ca-rich rim (~30 μm) (Fig. 4a, c).
431 These flat patterns are usually considered to indicate a high temperature, magmatic origin, unlike the
432 metamorphic garnet that show bell-shaped Mn compositional zoning (Dahlquist et al. 2007; Xia et al.
433 2017). (3) The REE patterns of the Grt_1 and Grt_2 crystals are comparable to those of the magmatic
434 garnet from typical S-type granites (Rong et al. 2018; Fig. 4d). (4) The absence of sillimanite in the
435 Yunlu charnockite also supports a magmatic origin of the garnet as the peritectic garnet commonly
436 coexists with various prograde metamorphic minerals such as sillimanite (Dorais et al. 2012).
437 Furthermore, the Grt_2 crystals were partly replaced, or surrounded by, anhedral Bt_2 + Qz_2
438 intergrowths around the grain boundaries, indicating a hydration crystallization reaction between
439 magmatic garnet and residual H_2O- and K_2O-rich melt (Beard et al. 2004, 2005) (Fig. 2e). In addition,
440 the different MnO contents of garnets from charnockite (Grt_1 and Grt_2) and the Bt-Grt gneiss
441 xenolith also exclude the possibility that Grt_1 and Grt_2 are xenocrysts (Fig. 4e). The slightly humped
442 REE patterns towards the rims of Grt_1 crystals may have resulted from preferential depletion of
443 HREEs from the rock-magma matrix during progressive garnet growth (Yu et al. 2016).

444 The orthopyroxene crystals (Opx_1 and Opx_2; Fig. 2c, d) in Yunlu garnet-bearing charnockite are

445 euhedral-anhedral with size of 0.5-6 mm. The Opx_1 crystals are mainly euhedral, which is different
446 from the orthopyroxenes in granulites with their subhedral to anhedral shapes and restricted grain
447 sizes (Harley et al. 1985; Tang et al. 2017). They classify as ferro-hypersthene (Fs = 49-56)
448 according to classification scheme of Morimoto (1988), and resemble orthopyroxenes that
449 crystallized from crust-derived felsic rocks (Clemens and Birch 2012; Shimura et al. 1992). The
450 orthopyroxene crystals have low Al_2O_3 contents with X_{Al} values of 0.012-0.086 and X_{Mg} values of
451 0.44-0.50, matching the magmatic orthopyroxenes from igneous charnockite (Fig. 5a). The mineral
452 paragenesis between orthopyroxene and biotite (orthopyroxene is commonly replaced/surrounded by
453 biotite) also precludes a metamorphic origin (Fig. 2c-e). Although Chen and Zhuang (1994)
454 identified both restitic and magmatic orthopyroxene based on their crystal shapes and mineral
455 inclusions, they have indistinguishable compositions (Fig. 5a). In addition, the minerals that form
456 inclusions (biotite and plagioclase) in the orthopyroxene crystals are the same, both in terms of
457 assemblage and composition, as those forming crystals in the charnockite (Appendix Table 1; Fig.
458 5d). This strongly supports a magmatic origin for both groups. The analyzed orthopyroxenes display
459 MREE-enriched patterns, which are different from the peritectic orthopyroxenes in granulite (Fig.
460 5b). The unusually low HREE contents of Opx_1 may be caused by the coexistence of Grt_1 which
461 consumed a significant proportion of HREEs from the magma.

462 The biotites of garnet-bearing charnockite have different geochemical characteristics from those
463 of Grt-Bt gneiss and gneissic granite xenoliths, ruling out the possibility that Bt_1 and Bt_2 are
464 xenocrysts (Appendix Table 1). Bt_1 and Bt_2 have identical compositions irrespective of their
465 occurrences (Fig. 5d). The Bt_1 crystals have euhedral shape and seldom contain mineral inclusions,
466 which indicates a magmatic origin. The Bt_2 crystals exhibit anhedral shapes and replace euhedral
467 Opx_1/Grt_1 crystals with Qz_2, forming an intergrowth texture (Fig. 2c, e). The presence of
468 orthopyroxene/garnet and ilmenite relicts in Bt_2 and the titaniferous nature of biotite also favor a
469 hydration crystallization reaction, i.e., orthopyroxene/garnet + ilmenite + melt → biotite + quartz

(Clemens and Wall 1988; Shimura et al. 1992; Bhowmik et al. 2009). To summarize, we believe that the Yunlu garnet-bearing charnockite is of igneous origin based on evidence from field outcrops, petrography and mineral chemistry.

6.1.2 Metamorphic overprint

The metamorphic overprint on Yunlu igneous charnockite is documented by the occurrences of garnet (Grt_3) + quartz (Qz_3) ± K-feldspar (Kfs_2) corona/symplectite textures at boundaries between plagioclase and ferromagnesian minerals (orthopyroxene, biotite, and ilmenite). The reactions are as follows:

$$Orthopyroxene\ (Opx_{1\&2}) + plagioclase\ (Pl_2) \rightarrow quartz\ (Qz_3) + garnet\ (Grt_3) \quad (1);$$

$$Biotite\ (Bt_{1\&2}) + plagioclase\ (Pl_2) \rightarrow quartz\ (Qz_3) + garnet\ (Grt_3) + K\text{-}feldspar\ (Kfs_2) \quad (2);$$

$$Ilmenite\ (Ilm) + plagioclase\ (Pl_2) \rightarrow quartz\ (Qz_3) + garnet\ (Grt_3) \quad (3);$$

All of the Grt_3 crystals in reaction (1) – (3) have lower MgO but higher CaO contents compared to Grt_1 and Grt_2 crystals (Fig. 4f). Meanwhile, although the Grt_3 crystals exhibit a range of REE patterns following reactions (1) – (3), they generally exhibit higher LREE and lower HREE contents than Grt_1 and Grt_2 (Fig. 4d). This may be related to the different REE contents of the reactive minerals (e.g., ilmenite, biotite, orthopyroxene). The geochemical characteristics, mineral distributions/ occurrences and paragenesis clearly support a sub-solidus (metamorphic) origin for the Grt_3 (Harley 1989). The Kfs_2 is anhedral (10-30 μm), associated with Grt_2 and Qz_3 and with Or contents of 91-94, and the Qz_3 coexists with Grt_3 and Kfs_2, with a size range of 20-50 μm. In view of grain size, shape, distribution, and chemical composition, we consider Qz_3 and Kfs_2 are both metamorphic origins (Fig. 3a-d). The Grt_3 has higher grossular but lower contents than Grt_1 and Grt_2, revealing an increase in pressure and decrease in temperature (Green 1976, 1977, 1992). The estimated P-T conditions of 710±100 MPa and 720-750±50 °C (Table 2) indicate a biotite dehydration reaction (2) during amphibolite-facies prograde metamorphism (Bhowmik et al. 2009). Despite the estimated P-T conditions for metamorphic overprint are indistinguishable within

uncertainties of thermobarometry from the estimated magmatic crystallization conditions at 610 ± 100 MPa and 780-820 ± 60 °C, it does not mean that the Yunlu charnockite has been totally reset or re-equilibrated by the metamorphic overprint. This is verified by the mineral zoning, e.g. oscillatory An zoning of magmatic Pl_1 and Ca-rich zoning of Grt_1 (Fig. 4c, e), and different mineral compositions of magmatic from metamorphic minerals, e.g. higher MgO, but lower CaO content for magmatic garnet (Grt_1 and Grt_2), and higher anorthite contents of the magmatic plagioclase (Pl_1).

Serval lines of micro-textural evidence also suggest that the influence of the amphibolite–facies metamorphic overprint is very limited, only forming the corona/symplectite texture at mineral boundaries (Fig. 3), but the igneous micro-textural and mineral chemical characteristics related to magmatic processes are largely preserved. Under the optical microscope, no pervasive granoblastic or re-equilibrium (sub-solidus grain-shape adjustment) textures have been observed in Yunlu charnockite. The polygonal crystal aggregate composed of quartz and plagioclase is minor in thin sections. Instead, the rock exhibits micro-textures typical of granitic rocks (Fig. 2c-f; Fig. S1 in supplementary material, Vernon (2008, 2010)). No inclusions of quartz and plagioclase with rounded shapes were identified. The rounded inclusions provide evidence for adjustment of their boundaries towards low energy configurations through the minimization of the interfacial area in granulites (Vernon 1968, 1999. No dehydration or melting reaction micro-textures that resemble those of metamorphic charnockite or granulite are observed in thin sections (Tang et al. 2017). This observation precludes the strong metamorphic overprint of the Yunlu charnockite, in which the biotite is replaced by orthopyroxene as a result of dehydration reactions during granulite-facies metamorphism (Vernon 2004). The general preservation of An normal and oscillatory zoning in plagioclase excludes extensive recrystallization or grain-boundary migration, as it would then be truncated or obliterated in granulite-facies metamorphism (Holness et al. 2018). Finally, the monazite crystals enclosed by Grt_3 record a late Devonian age (~370 Ma; Chen et al. 2012), while the zircons in garnet-bearing charnockite do not have overgrowths and yield an early Paleozoic age (~430 Ma;

520 Wang et al. 2013; Fig. S2 in supplementary material). This suggests that the temperature of
521 metamorphic overprint is enough to reset the monazite U-Pb systematics with closure temperature of
522 600-700 °C, but not enough to reset the zircon U-Pb systematics with higher closure temperature of
523 750-850 °C (Corfu 1988; Cherniak and Watson 2003; Smith and Giletti 1997). The metamorphic
524 overprint likely has temperature range of 700-750 °C, consistent with our estimation for
525 metamorphic overprint at 720-750 ± 50 °C (see Table 2).

526 In order to quantitively evaluate the influence of metamorphic event superimposed on the
527 mineral compositions in the Yunlu charnockite, we carry out a series of calculations to estimate
528 duration of the metamorphic event and diffusion lengths of key elements (used in thermobarometers)
529 in various minerals. Details of the modeling method and results are described in the supplementary
530 material. The results suggest that Ca-diffusion modeling of Grt_1 compositional profile constrains the
531 timescale of the late Devonian metamorphic event on an order of 0.2-0.5 Ma (Fig. 11a), which is
532 consistent with the timescale for an extremely short-duration metamorphism (<1.0 Ma, Viete and
533 Lister 2017). Under given metamorphic P-T condition (750 ℃, 710 MPa) and maximum duration of
534 ~0.5 Ma, we quantitatively evaluate the Fe-Mg inter-diffusion lengths in mafic minerals (garnet,
535 orthopyroxene and biotite), CaAl-NaSi interdiffusion length in plagioclase and Na-K inter-diffusion
536 length in K-feldspar, the calculation parameters and results are shown in Fig. 11b and supplementary
537 material. The calculated results show that only rim (<100 μm) of the mafic minerals are influenced
538 and reset by this thermal disturbance. The calculated diffusion distance in K-feldspar is ~ 4.0 mm
539 because of the fast Na-K inter-diffusion coefficient, while calculated diffusion length in plagioclase
540 is < 1.0 μm because of the extremely slow CaAl-NaSi inter-diffusion coefficient. Therefore, it is
541 believed that the magmatic crystallized compositions of the mafic minerals, plagioclase and core of
542 big K-feldspar crystals (grain size > 10 mm) are well preserved and have not reset by metamorphic
543 overprint.

544 The identification of a ~370 Ma amphibolite-facies metamorphic overprint in the Yunlu igneous

charnockite supports a regional thermal event in late Devonian. It has been also recognized in the rare metamorphic rocks (e.g., schist, gneiss, migmatite, amphibolite) exposed in northeastern region of the Cathaysia Block (Chen et al. 2018). However, the ~370 Ma thermal activity was mostly recorded by secondary monazites of rare metamorphic rocks and detrital zircons from Permian sedimentary rocks (Chen et al. 2018; Li et al. 2012). There are no reports of ~370 Ma felsic magmatism, and the coeval mafic magmatism was only found in the southern Zhejiang (an amphibolite with a Late Devonian crystallization age of ~370 Ma; Chen et al. 2018). The extremely short-duration of the late Devonian metamorphic event is generally interpreted as a result of local thermal turbulence with rapid tectonic burial and exhumation of relatively thin tectonic slices (Spear 2014). Nevertheless, more attention is needed to decipher the details of tectonic activity and thermal evolution in late Paleozoic.

6.2 Reconstruction of the crystallization processes

Magmatic fluids play an important role in magmatic crystallization (Scaillet et al. 2016; Scaillet and Macdonald 2001; Dall'Agnol et al. 1999; Costa et al. 2004). If granitic magma contains fluids with low H_2O activity, it solidifies under "hot" and "dry" conditions (Anderson et al. 2003; Harlov et al. 2013), e.g., at an elevated solidus temperature of 800-850 °C and low water activities of 0.3-0.5 at a pressure of ~400 MPa for the Thor Range intrusive complex from Antarctica (Bucher and Frost 2006). Conversely, if the granitic magma evolves under H_2O-rich fluid conditions, it will solidify at relatively "cold" and "wet" conditions (Shimura et al. 1992; Clemens and Birch 2012), e.g., under H_2O-saturated solidus conditions of ~670 °C and ~200 MPa for the peraluminous Jiuzhou charnockite from South China (Zhao et al. 2017). For the Yunlu garnet-bearing charnockite, fluid inclusions are not ubiquitous. Thirteen inclusions have been observed in both Qz_1 and Qz_2, and they are mostly H_2O-rich monophase inclusions (Fig. 6b). Only one inclusion in Qz_1 is characterized by a CO_2-H_2O mixture (Fig. 6a), implying that the CO_2 is a minor component in the fluid compositions of the Yunlu charnockite. This observation is analogous to the modeling results shown in Fig. 9, which

570 suggests that the exsolved fluids are CO_2-poor (~10 mol% CO_2 + ~90 mol% H_2O) at near-solidus
571 temperatures under 0.1 wt% CO_2 + 4.0 wt% H_2O conditions. Therefore, the scarcity of CO_2-rich fluid
572 and enrichment of H_2O-rich fluid suggest the Yunlu magma may contain ≤ 0.1 wt% CO_2. According
573 to the experimental-determined isobaric curve of mixed H_2O-CO_2 in rhyolitic melt at 600 MPa, the
574 CO_2 contents with ≤ 0.1 wt% have little influence on the H_2O solubility in rhyolitic melts (Papale et
575 al 2006; Duan et al 2014). We thus posit that H_2O will be the dominant fluid that control the phase
576 relationships and solidus temperature of the Yunlu charnockite.

577 Quartz and plagioclase stability fields depress with the increasing initial melt H_2O contents (Fig.
578 10; Clemens and Birch 2012; Clemens and Phillips 2014). According to the experimental data, quartz
579 and plagioclase crystallize earlier than garnet at melt H_2O of < 3.0 wt%, while they crystallize later
580 than garnet at ≥ 3.0 wt% melt H_2O at 500 MPa (T-$X^{Fl}H_2O$ diagram Fig. 14 of Clemens and Birch
581 2012). Our rhyolite-MELTS modeling also requires that the quartz and plagioclase crystallize later
582 than garnet at ≥ 4.0 wt% melt H_2O at ~600 MPa (Fig. 10). In the Yunlu charnockite, magmatic garnet
583 is euhedral and seldom contain euhedral quartz and plagioclase inclusions, indicating that garnet
584 crystallizes earlier than, or at the same time as, quartz and plagioclase. The initial melt H_2O thus
585 should be ~4.0 wt% according to the phase relationship modeling (Fig. 10). Besides, the geochemical
586 modeling results in section 5.1.2 also suggest a relatively high H_2O content (4.0 wt%). Therefore, we
587 posit that initial H_2O content of the Yunlu charnockite is ~4.0 wt%.

588 As discussed in section 5.1.1, the rhyolite-MELTS modeling cannot be used to predict
589 accurately the saturation temperatures of ferromagnesian minerals, given the errors of ≥ 100 °C. The
590 chosen sample MC01 in our modeling has a similar composition to that of the starting material LMI
591 9399 in Clemens and Birch's experiments (Table 3). They have similar SiO_2 contents (69.83 wt% vs.
592 68.15 wt%), ASI (1.11 vs. 1.10) and $Mg^{\#}$ values (38.9 vs. 36.7), and the pressures are also similar
593 (600 MPa vs. 500 MPa). Moreover, the oxygen fugacity in both our rhyolite-MELTS modeling and
594 Clemens and Birch's crystallization experiments is QFM-1. Given their similarities, the phase

595 relationships of ferromagnesian minerals in Clemens and Birch's experiments are used to calibrate
596 the rhyolite-MELTS modeling results in the following discussions.

597 At 4.0 wt% initial H_2O (Fig .10c), the orthopyroxene-in temperature is ~1077 °C according to
598 rhyolite-MELTS modeling, which is an unrealistic result for the granitic systems. Accordingly, the
599 orthopyroxene-in temperature is adjusted to 950 °C based on the experimental data from Clemens
600 and Birch (2012). The rhyolite-MELTS modeling predicts that orthopyroxene is stable until the
601 temperature decreases to ~777 °C, a result similar to ~800 °C at 500 MPa for LMI 9399 in Clemens
602 and Birch's experiments. Garnet starts to crystallize at ~887 °C and is stable down to the solidus
603 temperature as predicted by the rhyolite-MELTS modeling (Fig. 10c). This estimate is close to the
604 saturation temperature at ~920 °C of LMI 9399 in the experimental study (Clemens and Birch 2012).
605 Biotite is predicted to crystallize at ~777 °C. This value is constrained by the rhyolite-MELTS
606 modeling at 4.0 wt% initial H_2O (Fig. 10c), which is a significant underestimate (> 100 °C)
607 compared to the experimental data. As with the orthopyroxene, the biotite saturated temperature is
608 calibrated to 870 °C on the basis of experimental results from Clemens and Birch (2012). The
609 garnet-orthopyroxene ($Grt_{1,2}$-$Opx_{1,2}$), orthopyroxene-biotite ($Opx_{1,2}$-Bt_1) and garnet-biotite ($Grt_{1,2}$-Bt_1)
610 thermometers nevertheless yield approximate temperatures of ~770-820 °C, implying that
611 orthopyroxene, garnet and biotite didn't equilibrate at solidus temperatures (Fig. 12). Plagioclase and
612 quartz are predicted to saturate at ~877 °C and ~837 °C, based on the rhyolite-MELTS modeling at
613 4.0 wt% initial H_2O. This is simultaneous or slightly later than garnet. K-feldspar is the last phase to
614 crystallize and it saturates at ~757 °C in the modeling. Two-feldspar (Pl_1 rim-Kfs_1 core) thermometry
615 constrains the temperature to ~630 °C, which is consistent with the solidus temperature determined
616 by the experiments of Clemens and Birch (2012). The two-feldspar thermometry outlined above,
617 combined with fluid inclusion compositions, require that the Yunlu magma solidified at the
618 H_2O-saturated solidus (630 °C) at 600 MPa (Fig. 12). It is believed that the igneous charnockite
619 usually represents a high temperature ("hot"), H_2O-unsaturated ("dry") magma because of the

presence of orthopyroxene. However, the above temperature and melt H_2O content estimates demonstrate that the Yunlu garnet-bearing charnockite finally solidified under "cold" and "wet" conditions. In addition, the Yunlu charnockite contained high initial H_2O contents (~4.0 wt%). We propose that, at intermediate H_2O contents, the granitic magma could crystallize orthopyroxene as well, even if it may be consumed by residual melt to produce biotite + quartz (Bt_2 + Qz_2).

6.3 Melt extraction of the Yunlu garnet-bearing charnockite: Insight from mineral thermometry

Plutonic rocks commonly crystallize at slow cooling rates with prolonged crystallization histories compared with their volcanic equivalents (Holness et al. 2018), which allows more efficient element exchange and chemical equilibration between minerals and melt. Hence, the major element-based mineral-pair thermometers for intrusive rocks should record solidus or near-solidus temperatures. However, a wealth of thermometric studies on some granitic batholiths yields a large range of temperature estimations (Shimura et al. 1992; Wang et al. 2018; Elliott et al. 1998; Moazzen and Droop 2005), indicating that equilibrium crystallization near the (H_2O-saturated) solidus may not always happen (Anderson 1996, 2008). Disequilibrium may be caused by recharge of more primitive, high-temperature magma, which produces high-temperature domains within partial dissolution and/or resorption of minerals (e.g. orthopyroxene, garnet and plagioclase; Day et al., 1992; Nxion 1988; Pietranik et al. 2006; Shcherbakov et al., 2011). Such disequilibrium features may be well preserved in shallow-emplaced granites and small volume intrusions (e.g., granitic dikes, Pietranik et al. 2006).

For the Yunlu charnockite, the rhyolite-MELTS modeling and the two-feldspar thermometer constrain the solidus temperature of Yunlu charnockite is ~630 °C, which is consistent with the experimental-determined H_2O-saturated solidus temperature of granitic rocks of ~600-650 °C at 600 MPa (Johannes and Holtz 1996; Ebadi and Johannes 1991; Huang and Wyllie 1973; Tuttle and Bowen 1958). Nevertheless, garnet-orthopyroxene, garnet-biotite and orthopyroxene-biotite Fe-Mg

exchange thermometers yield temperatures of ~820 ± 50 °C, ~770 ± 50 °C and ~780 ± 60 °C, respectively, which are significantly above the H_2O-saturated solidus. The $Mg^{\#}$ values of magmatic garnet and orthopyroxene ($Grt_{1,\ 2}$ & $Opx_{1,\ 2}$) lie along experimentally calibrated arrays, supporting equilibrated Fe-Mg partitioning between the early crystallized garnet and orthopyroxene (Fig. 5c). In other words, the early crystallized ferromagnesian minerals equilibrate at a temperature range of 770-820 °C, which instead equilibrate at the H_2O-saturated solidus (Fig. 12). The higher equilibrium temperature for the early crystallized ferromagnesian minerals is not likely caused by metamorphic overprint as suggested by the clear distinct mineral compositions between magmatic ($Grt_{1,\ 2}$ and Pl_1) and metamorphic origin (Grt_3 and Pl_2) and compositional zoning of garnet and plagioclase (Fig. 4, 5).

For the Yunlu charnockite with depth of emplacement (~20 km), a very slow cooling rate and prolonged crystallization process should be in favor of magma equilibrium at near-solidus temperatures. The absence of partial dissolution and/or resorption texture as well as the Mg- or Ca-rich rims for the early crystallized minerals, e.g. garnet, orthopyroxene, plagioclase, and the normal An zoning of plagioclase further collectively suggest an closed-system, equilibrium crystallization of these early crystallized phases. Generally, the consistency temperatures derived from different Fe-Mg exchange thermometers could be result from loss of a pervasive transport medium, such as a melt or fluid, because chemical equilibration is easy to achieve due to the fast diffusion rate in the interstitial melt (Pattison and Begin 1994a, 1994b). One possible hypothesis is that extraction of interstitial melt from a highly crystalline framework (the so-called “crystal mush”) took place in the Yunlu magma chamber continuously at 770-820 °C, which physically segregates the crystallized minerals from the interstitial melt. This leads to pervasive contact among the minerals, thus chemical equilibrium is difficult to achieve because of the diffusion barrier at grain boundaries, especially when ferromagnesian minerals are in contact with quartz and feldspar (Pattison and Begin 1994a). Therefore, the compositions of the mafic minerals will be in equilibrium with co-existed

interstitial melt at the temperature of melt extraction, which is constrained at ~780-820 °C with corresponding crystallinities of ~30-45 % (the orthopyroxene will be consumed below 777 °C) (Fig. 10, 12) (Bachmann and Bergantz 2004, 2006, 2008). After the majority of the interstitial melt is expulsed, the less amount of residual melt would crystallize K-feldspar and the overgrowths of the quartz and plagioclase (Zhao et al., 2018). Hence, the K-feldspar, being the last mineral to crystallize, thus would be in equilibrium with plagioclase rim at near solidus temperature. Using the rim composition of plagioclase and core composition of big K-feldspar, the two-feldspar thermometer yields a near solidus temperature of ~630 °C (Fig. 12). Melt extraction can be supported by the micro-texture evidence (Fig. 2f), the significant accumulation of plagioclase, garnet and orthopyroxene crystals under thin sections supports the existence of melt extraction (Fig. 2e, f). Besides, locally high concentrations of euhedral to subhedral plagioclase crystals form a framework with interstitial quartz crystals and so explain the cumulate texture of the Yunlu charnockite (Fig. 2f; Vernon and Collins 2011).

7. Implications

In some granitic plutons, the calculated temperatures by mineral thermometry are higher than experimentally-determined H_2O-saturated solidus temperatures. Although various models have been proposed, e.g., non-equilibrium crystallization, high-temperature magma recharge and post-magmatic metamorphic overprints, this discrepancy remains controversial and restricts the application of granite thermometry. Here, the near consistent temperatures (~780-820 °C) obtained for the Yunlu garnet-bearing charnockite constrained by garnet-orthopyroxene, garnet-biotite and orthopyroxene-biotite Fe-Mg exchange thermometers significantly deviate from its experimental solidus temperature (~630 °C). This higher temperature recorded by ferromagnesian minerals (i.e., orthopyroxene, garnet and biotite) may result from melt extraction of the interstitial melt in a crystal mush at 30-45 % crystallinity (Fig. 12). This interpretation is also supported by the cumulate textures and the geochemical modeling of the whole-rock compositions of the charnockite. In addition, the

695 influence of melt extraction on the application of mineral thermometers and the interpretation of
696 thermometry data should be carefully reconsidered in granitic plutons.

697 The widely applied rhyolite-MELTS modeling has been rigorously compared with experimental
698 petrology studies of metaluminous, silicic volcanic systems under low pressure (≤ 300 MPa)
699 conditions (Gardner et al. 2014). However, it had never been evaluated and compared with
700 experimental data for peraluminous magma systems at higher pressures (> 300 MPa). Here, we
701 carried out a rigorous comparison between modeling results of rhyolite-MELTS and experimental
702 petrology data on a peraluminous ignimbrite at 500 MPa in order to estimate its uncertainties. Our
703 study shows that rhyolite-MELTS modeling can predict phase relationships for quartz and two
704 feldspars within reasonable limits (≤ 60 °C) at ≤ 7.0 wt% H_2O, but that it poorly constrains the phase
705 saturation temperatures for the ferromagnesian minerals (≥ 100 °C). Hence, the rhyolite-MELTS
706 software may need modifications in the future to better constrain the saturation curves of the
707 ferromagnesian minerals.

708 The high emplacement temperature (900 °C) and pressure (600 MPa) of the Yunlu charnockite
709 require a high geothermal gradient (> 45 °C/km) in the Yunkai terrane, in which the melting
710 temperature in the source (lower crust) exceeds 900 °C. Radiogenic heating in thickened crust is
711 inadequate to supply such a high heat flux (Xu and Xu 2015; Xia et al. 2014). The heat from deep
712 mantle is necessary, such as via basaltic magma underplating and asthenospheric upwelling followed
713 by post-orogenic collapse and lithospheric thinning of the early Paleozoic intra-continental orogen in
714 the SCB (Huang et al. 2013; Zhong et al. 2016; Yu et al. 2018). Furthermore, an extremely
715 short-duration (~0.5 Ma), amphibolite-facies (750 °C, 710 MPa), late Devonian thermal event is
716 recognized in this region (Chen et al. 2012, 2018; this study). However, its geodynamic mechanism
717 still remains controversial. Spear (2014) proposed that the short-duration metamorphic event requires
718 rapid tectonic burial of relatively thin tectonic slices. Based on the duration of the late Devonian
719 metamorphic event, we speculate that it may result from the local thermal turbulence with rapid

tectonic burial and exhumation of thin nappe tectonic complexes. However, further work related to this late Devonian metamorphism needs to be implemented to document its tectonic significance.

Acknowledgements

This work was financially supported by the National Natural Science Foundation of China (Grants 41430208 and 41602046). We thank Bruno Scaillet and two anonymous reviewers for their comments and suggestions that have helped improve this paper significantly. Further thanks go to Christy Till's editorial effort and constructive comments. We also appreciate Julian Pearce for helpful discussion and language polishing.

References cited

Acosta-Vigil, A., Rubatto, D., Bartoli, O., Cesare, B., Meli, S., Pedrera, A., Azor, A., and Tajčmanová, L. (2014) Age of anatexis in the crustal footwall of the Ronda peridotites, S Spain. Lithos, 210-211, 147-167.

Anderson, J.L. (1996) Status of thermobarometry in granitic batholiths. Transactions of the Royal Society of Edinburgh: Earth Sciences, 87, 125-138.

Anderson, I.C., Frost C.D., and Frost B.R. (2003) Petrogenesis of the red mountain pluton, Laramie anorthosite complex, wyoming: implications for the origin of A-type granite. Precambrian Research, 124, 243–267.

Anderson, J.L., Barth A.P., Wooden J.L., and Mazdab F. (2008) Thermometers and thermobarometers in granitic systems. Reviews in Mineralogy and Geochemistry, 69, 121-142.

Annen, C., Blundy, J.D., and Sparks, R.S.J. (2006) The genesis of intermediate and silicic magmas in deep crustal hot zones. Journal of Petrology, 47, 505–539.

Aranovich, L.Ya., Lavrent'eva, I.V., and Kosyakova, N.A. (1988) Calibration of the biotite-garnet and biotite-orthopyroxene geothermometers corrected for the variable level in biotite. Geochemistry International, 25, 50–59.

Asimow, P. D. and Ghiorso, M. S. (1998) Algorithmic modifications extending MELTS to calculate

745 subsolidus phase relations. American Mineralogist, 83, 1127-1132.

746 Baba, S. (1999) Sapphirine-bearing orthopyroxene-kyanite/sillimanite granulites from South Harris,
747 NW Scotland: Evidence for Proterozoic UHT metamorphism in the Lewisian. Contributions to
748 Mineralogy and Petrology, v. 136, p. 33–47.

749 Bachmann, O., and Bergantz, G.W. (2004) On the origin of crystal-poor rhyolites: extracted from
750 batholithic crystal mushes. Journal of Petrology, 45, 1565–1582.

751 Bachmann, O., and Bergantz, G.W. (2006) Gas percolation in upper-crustal silicic crystal mushes as
752 a mechanism for upward heat advection and rejuvenation of near-solidus magma bodies. Journal
753 of Volcanology and Geothermal Research, 149, 85–102.

754 Bachmann, O., and Bergantz, G.W. (2008) Deciphering magma chamber dynamics from styles of
755 compositional zoning in large silicic ash flow sheets. Reviews in Mineralogy and Geochemistry,
756 69, 651–674.

757 Bachmann, O., Deering, C.D., Ruprecht, J.S., Huber, C., Skopelitis, A., and Schnyder, C. (2012)
758 Evolution of silicic magmas in the Kos-Nisyros volcanic center, Greece: A petrological cycle
759 associated with caldera collapse. Contributions to Mineralogy and Petrology, 163, 151–166.

760 Bachmann, O., and Huber, C. (2016) Silicic magma reservoirs in the Earth's crust. American
761 Mineralogist, 101, 2377–2404.

762 Bartoli, O., Cesare, B., Remusat, L., Acosta-Vigil, A., and Poli, S. (2014) The H_2O content of granite
763 embryos. Earth and Planetary Science Letters, 395, 281–290.

764 Beard, J.S., Ragland, P.C., and Rushmer, T. (2004) Hydration crystallization reactions between
765 anhydrous minerals and hydrous melt to yield amphibole and biotite in igneous rocks:
766 description and implications. The Journal of Geology, 112, 617–621.

767 Beard, J.S., Ragland, P.C., and Crawford, M.L. (2005) Reactive bulk assimilation: A model for
768 crust-mantle mixing in silicic magmas. Geology, 33, 681–684.

769 Berman, R. G., and Bostock, H. H. (1997) Metamorphism in the northern Taltson magmatic zone,

Northwest Territories. The Canadian Mineralogist, v. 35, p. 1069–1091.

Best, M.G. (2003) Igneous and Metamorphic Petrology 2nd edition, 729p. Blackwell Science Ltd, UK.

Bhattacharya, A., Krishnakumar, K.R., Raith, M., and Sen, S.K. (1991) An improved set of a-X parameters of Fe-Mg-Ca garnets and refinements of the orthopyroxene–garnet thermometer and the orthopyroxene-garnet-plagioclase-quartz barometer. Journal of Petrology, 32, 629–656.

Bhowmik, S.K., Saha, L., Dasgupta, S., and Fukuoka, M. (2009) Metamorphic phase relations in orthopyroxene-bearing granitoids: implication for high-pressure metamorphism and prograde melting in the continental crust. Journal of Metamorphic Geology, 27, 295-315.

Bucher, K., and Frost, B.R. (2006) Fluid transfer in high-grade metamorphic terrains intruded by anorogenic granites: the Thor Range, Antarctica. Journal of Petrology, 47, 567–593.

Carrington, D.P., and Harley, S.L. (1995) Partial melting and phase relations in high-grade metapelites: an experimental petrogenetic grid in the KFMASH system. Contributions to Mineralogy and Petrology, 120, 270–291.

Cashman, K.V., Sparks, R.S.J., and Blundy, J.D. (2017) Vertically extensive and unstable magmatic systems: a unified view of igneous processes. Science, 355, 1280.

Chen, B., and Zhuang, Y.X. (1994) The petrology and petrogenesis of Yunlu charnockite and its granulite inclusion, west Guangdong, South China. Acta Petroligica Sinica, 10, 139–150. (In Chinese with English abstract)

Chen, C.H., Liu, Y.H., Lee, C.Y., Xiang, H., and Zhou, H.W. (2012) Geochronology of granulite, charnockites, and gneiss in the poly-metamorphosed Gaozhou Complex (Yunkai massif), South China: emphasis on the in-situ EMP monazite dating. Lithos, 144–145, 109–129.

Chen, C. H., Lee, C. Y., Liu, Y. H., Xiang, H., Zeng, W., and Zhou, H. W. (2018) Precambrian Protoliths and Phanerozoic overprinting on the Wuyishan terrain (South China): new evidence from a combination of LA-ICPMS zircon and EMP monazite geochronology. Precambrian

795 Research, 307, 229–25.
796 Cherniak, D.J., Watson, E.B. (2003) Diffusion in zircon. Reviews in Mineral & Geochemistry, 53,
797 113-143
798 Claeson, D.T., (1998) Coronas, reaction rims, symplectites and emplacement depth of the Rymmen
799 gabbro, Trans-Scandinavian igneous belt, southern Sweden. Mineralogical Magazine, 62,
800 743-757.
801 Clemens, J.D. (1984) H_2O content of silicic to intermediate magmas. Lithos, 17, 273-287.
802 Clemens, J.D., and Wall, V.J. (1988) Controls on the mineralogy of S-group volcanic and plutonic
803 rocks. Lithos, 21, 53–66.
804 Clemens, J.D., and Birch, W.D. (2012) Assembly of a zoned volcanic magma chamber from multiple
805 magma batches: the Cerberean Cauldron, Marysville Igneous Complex, Australia. Lithos, 155,
806 272-288.
807 Clemens, J.D., and Phillips, G.N. (2014) Inferring a deep-crustal source terrane from a high-level
808 granitic pluton: the Strathbogie Batholith, Australia. Contributions to Mineralogy and Petrology,
809 168, 1–22.
810 Costa, F., Scaillet, B., and Pichavant, M. (2004) Petrological and experimental constraints on
811 pre-eruption conditions of Holocene dacite from volcanic San Pedro (36 °S, Chilean Andes) and
812 the importance of sulphur in silicic subduction-related magmas. Journal of Petrology, 45,
813 855-881.
814 Conrad, W.K., Nicholls, I.A., and Wall, V.J. (1988) Water-saturated and -undersaturated melting of
815 metaluminous and peraluminous crustal compositions at 10 kbar: evidence for the origin of
816 silicic magmas in the Taupo Volcanic Zone, New Zealand, and other occurrences. Journal of
817 Petrology, 29, 765–803.
818 Corfu, F. (1988) Differential response of U-Pb systems in coexisting accessory minerals, Winnipeg
819 River Subprovince, Canadian Shield: implications for Archean crustal growth and stabilization.

Contributions to Mineralogy and Petrology, 98, 312-325.

Dahlquist, J.A., Galindo, C., Pankhurst, R.J., Rapela, C.W., Alasino, P.H., Saavedra, J., and Fanning, C.M. (2007) Magmatic evolution of the Peñón Rosado granite: petrogenesis of garnet-bearing granitoids. Lithos, 95, 177–207.

Dall'Agnol, R., Scaillet, B., and Pichavant, M. (1999) An experimental study of a lower Proterozoic A-type granite from the Eastern Amazonian Craton, Brazil. Journal of Petrology, 40, 1673-1698.

Day, R.A., Green, T.H., and Smith, I.E.M. (1992) The origin and significance of garnet phenocrysts and garnet-bearing xenoliths in Miocene calcalkaline volcanics from Northland, New Zealand. Journal of Petrology, 33, 125–161.

Dempster, T. J., Harrison, T. N., Brown, P. E., and Hutton, D. H. W. (1991) Low-pressure granulites from the Ketilidian mobile belt of southern Greenland. Journal of Petrology, 32, 979–1004.

Dorais, M.J., Pett, T.K., and Tubrett, M. (2009) Garnetites of the Cardigan Pluton, New Hampshire: evidence for peritectic garnet and implications for source rock compositions. Journal of Petrology, 50, 1993–2016.

Dorais, M.J., and Tubrett, M. (2012) Detecting peritectic garnet in the peraluminous Cardigan pluton, New Hampshire. Journal of Petrology, 53, 299–324.

Dorais, M.J., and Spencer, C.J. (2014) Revisiting the importance of residual source material (restite) in granite petrogenesis: the Cardigan Pluton, New Hampshire. Lithos, 202, 237–249.

Duan, X.Z. (2014) A general model for predicting the solubility behavior of H_2O–CO_2 fluids in silicate melts over a wide range of pressure, temperature and compositions. Geochemical et Cosmochimica Acta, 125, 582–609

Ebadi, A., and Johannes, W. (1991) Beginning of melting and composition of first melts in the system Qz-Ab-Or-H_2O-CO_2. Contributions to Mineralogy and Petrology, 106, 286–295.

Eggins, S., and Hensen, B.J. (1987) Evolution of mantle-derived, augite-hypersthene granodiorites

by crystal-liquid fractionation: barrington Tops Batholith, eastern Australia. Lithos, 20, 295–310.

Elliott, B.A., Ramo, O.T., and Nironen, M. (1998) Mineral chemistry constraints on the evolution of the 1.88-1.87 Ga post-kinematic granite plutons in the Central Finland Granitoid Complex. Lithos, 45, 109-129.

Elkins, L.T., and Grove, T.L. (1990) Ternary feldspar experiments and thermodynamic models. American Mineralogist, 75, 544-559.

Fiedrich, A.M., Bachmann, O., Ulmer, P., Deering, C.D., Kunze, K., and Leuthold, J. (2017) Mineralogical, geochemical, and textural indicators of crystal accumulation in the Adamello Batholith (Northern Italy). American Mineralogist, 102, 2467-2483.

Fuhrman, M.L., and Lindsley, D.H. (1988) Ternary-feldspar modeling and thermometry. American Mineralogist, 73, 201-215.

Frost, C.D., Frost, B.R., Chamberlain, K.R., and Edwards, B.R. (1999) Petrogenesis of the 1.43 Ga Sherman batholith, SE Wyoming: a reduced rapakivi-group anorogenic granite. Journal of Petrology, 40, 1771-1802.

Frost, B.R., Frost, C.D., Hulsebosch, T.P., and Swapp, S.M. (2000) Origin of the charnockites of the Louis Lake batholith, Wind River Range, Wyoming. Journal of Petrology, 41, 1759-1776.

Frost, B.R and Frost, C.D. (2008). On charnockites. Gondwana Research, 13, 30-44.

Gardner, J., Befus, K., Gualda, G.R., and Ghiorso, M. (2014) Experimental constraints on rhyolite-MELTS and the Late Bishop Tuff magma body. Contributions to Mineralogy and Petrology, 168, 1-14.

Ghiorso, M.S. (1984) Activity/composition relations in the ternary feldspars. Contributions to Mineralogy and Petrology, 87, 282-296.

Ghiorso, M. S., and Sack, R. O. (1995) Chemical mass-transfer in magmatic processes. 4. A revised and internally consistent thermodynamic model for the interpolation and extrapolation of

liquid-solid equilibria in magmatic systems at elevated temperatures and pressures. Contributions to Mineralogy and Petrology, 119, 197-212.

Ghiorso, M.S., and Gualda, G.A.R. (2015) An H_2O-CO_2 mixing fluid saturation model compatible with rhyolite-MELTS. Contribution to Mineralogy and Petrology, 169, 1-30.

Grabau, A.W. (1924) Stratigraphy of China, Part I, Paleozoic and older. The Geological Survey of Agriculture and Commerce, 528. Peking 1–6.

Green, T.H. (1976) Experimental generation of cordierite- or garnet-bearing granitic liquids from a pelitic composition. Geology, 4, 85–88.

Green, T. H. (1977) Garnet in silicic liquids and its possible use as a P-T indicator. Contributions to Mineralogy and Petrology, 65, 59–67.

Green, T.H. (1992) Experimental phase equilibrium studies of garnet-bearing I-group volcanic and high-level intrusives from Northland, New Zealand. Transactions of the Royal Society of Edinburgh: Earth Sciences, 83, 429–438.

Gualda, G.A.R., Ghiorso, M.S., Lemons, R.V., and Carley, T.L. (2012) Rhyolite-MELTS: a modified calibration of MELTS optimized for silica-rich, fluid-bearing magmatic systems. Journal of Petrology, 53, 875–890.

Gualda, G.A.R., and Ghiorso, M.S. (2013) The Bishop Tuff giant magma body: An alternative to the Standard Model. Contributions to Mineralogy and Petrology, 166, 755–775.

Gualda, G.A.R., and Ghiorso, M.S. (2015) MELTS_Excel: A Microsoft Excel-based MELTS interface for research and teaching of magma properties and evolution. Geochemistry, Geophysics, Geosystem, 16, 315-324.

Hansen, E.C., Janardhan, A.S., Newton, R.C., Prame, W.K.B.N., and Ravindra Kumar, G.R. (1987) Arrested charnockite formation in southern India and Sri Lanka. Contributions to Mineralogy and Petrology, 96, 225-244.

Harley, S.L. (1985) Garnet-orthopyroxene bearing granulites from Enderby Land, Antarctica:

metamorphic pressure– temperature–time evolution of the Archaean Napier Complex. Journal of Petrology, 26, 819–856.

Harley, S.L. (1989) The origin of granulites: a metamorphic perspective. Geological Magazine, 126, 215–247.

Harley, S. L., Hensen, B. J., and Sheraton, J. W. (1990) Two-stage decompression in orthopyroxene–sillimanite granulites from Forefinger Point, Enderby Land, Antarctica: Implications for the evolution of the Archaean Napier Complex: Journal of Metamorphic Geology, v. 8, p. 591–613.

Harlov, D.E., van den Kerkhof, A., and Johansson, L. (2013) The Varberg-Torpa Charnockite-Granite Association, SW Sweden: mineralogy, petrology, and fluid inclusion chemistry. Journal of Petrology, 54, 3–40.

Harlov, D.E., van den Kerkhof, A., and Johansson, L. (2014) Localized, solid-state dehydration associated with the Varberg charnockite intrusion, SW Sweden. Precambrian Research, 253, 50–62.

Hartung, E., Caricchi, L., Floess, D., Wallis, S., Harayama, S., Kouzmanov, K., and Chiaradia, M. (2017) Evidence for residual melt extraction in the Takidani Pluton, Central Japan. Journal of Petrology, 58, 763–788.

Henry, D.J., and Guidotti, C.V. (2002) Titanium in biotite from metapelitic rocks: temperature effects, crystal-chemical controls, and petrologic applications. American Mineralogist, 87, 375–382.

Henry, D.J., Guidotti, C.V., and Thomson, J.A. (2005) The Ti-saturation surface for low-to-medium pressure metapelitic biotites: implications for geothermometry and Ti-substitution mechanisms. American Mineralogist, 90, 316–328.

Hertogen, J., and Mareels, J. (2016) SilMush: a procedure for modeling of the geochemical evolution of silicic magmas and granitic rocks. Geochimica et Cosmochimica Acta, 185, 498–527.

Holdaway, M.J. (2000) Application of new experimental and garnet Margules data to the garnet-biotite geothermometer. American Mineralogist, 85, 881–892.

Holdaway, M.J. (2001) Recalibration of the GASP geobarometer in light of recent garnet and plagioclase activity models and versions of the garnet–biotite geothermometer. American Mineralogist, 86, 1117–1129.

Holtz, F., Johannes, W., Tamic, N., and Behrens, H. (2001) Maximum and minimum water contents of granitic melts: a re-examination and implications. Lithos, 56, 1–14.

Holness, M.B., Clemens, J.D., and Vernon, R.H. (2018) How deceptive are microstructures in granitic rocks? Answers from integrated physical theory, phase equilibrium, and direct observations. Contributions to Mineralogy and Petrology, 173, 2–18.

Huang, W.L., and Wyllie, P.J. (1973) Melting relations of muscovite-granite to 35 kbar as a model for fusion of metamorphosed subducted oceanic sediments. Contributions to Mineralogy and Petrology, 42, 1–14.

Johannes, W., and Holtz, F. (1996) Petrogenesis and Experimental Petrology of Granitic Rocks. 335 p. Springer, Germany.

Lavaure, S., and Sawyer, E.W. (2011) Source of biotite in the Wuluma Pluton: Replacement of ferromagnesian phases and disaggregation of enclaves and schlieren. Lithos, 125, 757–780.

Le Maitre, R.R.W., 2002. Igneous rocks: a classification and glossary of terms. Recommendations of the International Union of Geological Sciences, Sub commission on the Systematics of Igneous. Cambridge University Press, Rocks.

Lee, C.T., Morton, D.M., Farner, M.J., and Moitra, P. (2015) Field and model constraints on silicic melt segregation by compaction/hindered settling: The role of water and its effect on latent heat release. American Mineralogist, 100, 1762–1777.

Li, Z.X., Li, X.H., Wartho, J.A., Clark, C., Li, W.X., Zhang, C.L., and Bao, C.M. (2010). Magmatic and metamorphic events during the Early Paleozoic Wuyi–Yunkai orogeny, southeastern South China: New age constraints and P–T conditions. Geological Society of America Bulletin, 122, 772–793.

945 Li, L.M., Sun, M., Wang, Y.J., Xing, G.F., Zhao, G.C., Lin, S.F., Xia, X.P., Chan, L.S., Zhang, F.F.,
946 and Wong, J. (2011) U–Pb and Hf isotopic study of zircons from migmatised amphibolites in
947 the Cathaysia Block: implications for the early Paleozoic peak tectonothermal event in
948 Southeastern China. Gondwana Research, 19, 191–201.
949 Li, X.H., Li, Z.X., He, B., Li, W.X., Li, Q.L., Gao, Y., and Wang, X.C. (2012) The Early Permian
950 active continental margin and crustal growth of the Cathaysia Block: in situ U-Pb, Lu-Hf and O
951 isotope analyses of detrital zircons. Chemical Geology, 328, 195–207.
952 Lin, W., Wang, Q.C., and Chen, K. (2008) Phanerozoic tectonics of south China block: new insights
953 from the polyphase deformation in the Yunkai massif. Tectonics, 27, TC6004.
954 Lindsley, D.H., and Frost, B.R. (1992) Equilibria among Fe–Ti oxides, pyroxenes, olivine, and
955 quartz: Part I. Theory. American Mineralogist, 77, 987–1003.
956 Ma, X., Fan, H.R., Santosh, M., and Guo, J. (2013) Geochemistry and zircon U–Pb chronology of
957 charnockites in the Yinshan Block, North China Craton: tectonic evolution involving
958 Neoarchaean ridge subduction. International Geology Review, 55, 1688–1704.
959 Mikhalsky, E., and Kamenev, I. (2013) Recurrent transitional group charnockites in the east Amery
960 Ice Shelf coast (East Antarctica): petrogenesis and implications on tectonic evolution. Lithos,
961 175–176, 230–243.
962 Morimoto, N. (1988) Nomenclature of pyroxenes. Mineralogy and Petrology, 39, 55–76.
963 Moazzen, M., and Droop, G.T.R. (2005) Application of mineral thermometers and barometers to
964 granitoid igneous rocks: the Etive Complex, W Scotland. Mineralogy and Petrology, 83, 27-53.
965 Montel, J. M., and Vielzeuf, D. (1997) Partial melting of metagreywacke, Part II. Compositions of
966 minerals and melts. Contributions to Mineralogy and Petrology, 128, 176–196.
967 Naney, M.T. (1983) Phase equilibria of rock-forming ferromagnesian silicates in granitic systems.
968 American Journal of Science, 283, 993–1033.
969 Narduzzi, F., Farina, F., Stevens, G., Lana, C., and Nalini-Jr, H.A. (2017) Magmatic garnet in the

Cordilleran-group Galiléia granitoids of the Araçuaí belt (Brazil): Evidence for crystallization in the lower crust. Lithos, 283, 82-97.

Nair, R., and Chacko, T. (2002) Fluid-absent melting of high-grade semi-pelites: P-T constraints on orthopyroxene formation and implications for granulite genesis. Journal of Petrology, 43, 2121-2142.

Newton, R.C., and Tsunogae, T. (2014) Incipient charnockite: characterization at the type localities. Precambrian Research, 253, 38-49.

Newman, S., and Lowenstern, J.B. (2002) VolatileCalc: a silicate melt–H_2O–CO_2 solution model written in Visual Basic for Excel. Computer & Geoscience, 28, 597–604.

Nishimura, K., and Yanagi, T. (2000) In situ fractional crystallization observed in the Osumi granodiorite batholith. Earth and Planetary Science Letters. 180, 185–199.

Nixon, G. T., (1988) Petrology of the younger andesites and dacites of Iztaccihuatl Volcano, Mexico: I. Disequilibrium phenocryst assemblages as indicators of magma chamber processes. Journal of Petrology, 29, 213-64

Papale, P., Moretti, R., and Barbato, D. (2006) The compositional dependence of the saturation surface of $H_2O + CO_2$ fluids in silicate melt. Chemical Geology. 229, 78–95

Patino Douce, A. E. and Beard, J. S. (1996). Effect of P, $f(O_2)$ and Mg/Fe ratio on dehydration melting of model metagreywackes. Journal of Petrology, 37, 999–1024.

Pattison, D.R.M. and Begin, N.J. (1994a) Zoning patterns in orthopyroxene and garnet in granulites: implications for geothermometry. Journal of Metamorphic Geology, 12, 387–410.

Pattison, D.R.M., and Begin, N.J. (1994b) Hierarchy of closure temperatures in granulites and the importance of an intergranular exchange medium (melt?) in controlling maximum Fe-Mg exchange temperatures, Mineralogical Magazine. 58, 694-695.

Pamukcu, A.S., Carley, T.L., Gulada, G.A.R., Miller, C.F., and Ferguson, C.A. (2013) The evolution of the Peach Spring giant magma body: Evidence from accessory mineral textures and

995 compositions, bulk pumice and glass geochemistry, and rhyolite-MELTS modeling. Journal of
996 Petrology, 54, 1109–1148.
997 Pietranik, A., Koepke, J., and Puziewicz, J. (2006) The study of crystallization and resorption in
998 plutonic plagioclase: implications on evolution of granodiorite magma (Gesiniec granodiorite,
999 Strzelin Crystalline Massif, SW Poland). Lithos, 86, 260-280.
1000 Putirka, K.D. (2008) Thermometers and barometers for volcanic systems. Reviews in Mineral &
1001 Geochemistry, 69, 61-120.
1002 Qiu, X.F., Zhao, X.M., Yang, H.M., Lu, S.S., Jiang, T., and Wu, N.W. (2018) Petrogenesis of the
1003 early Paleozoic granitoids from the Yunkai massif, South China Block: Implications for a
1004 tectonic transition from compression to extension during the Caledonian orogenic event.
1005 Geological Magazine, 2017, 1–17.
1006 Rajesh, H.M., Santosh, M., and Yoshikura, S. (2011) The Nagercoil Charnockite: a magnesian, calcic
1007 to calc-alkaline granitoid dehydrated during a granulite-facies metamorphic event. Journal of
1008 Petrology, 52, 375–400.
1009 Rajesh, H.M., and Santosh, M. (2012) Charnockites and charnockites. Geoscience Frontiers, 6,
1010 737-744.
1011 Rong, W., Zhang, S. B., Zheng, Y. F., and Gao, P. (2018) Mixing of felsic magmas in granite
1012 petrogenesis: Geochemical records of zircon and garnet in peraluminous granitoids from South
1013 China. Journal of Geophysical Research: Solid Earth, 123, 2738–2769.
1014 Saha, L., Bhowmik, S. K., Fukuoka, M., and Dasgupta, S. (2008) Contrasting episodes of regional
1015 granulite facies metamorphism in enclaves and host gneisses from the Aravalli-Delhi Mobile
1016 Belt, NW India. Journal of Petrology, 49, 107–128.
1017 Santosh, M., Harris, N.B.W., Jackson, D.H., Mattey, D.P. (1990) Dehydration and incipient
1018 charnockite formation: a phase equilibria and fluid inclusion study from South India. Journal of
1019 Geology, 98, 915-926.

1020 Scaillet, B., Pichavant, M., and Roux, J. (1995) Experimental crystallization of leucogranite magmas.
1021 Journal of Petrology, 36, 663-705.
1022 Scaillet, B., and Macdonald, R. (2001) Phase relations of peralkaline silicic magmas and petrogenetic
1023 implications. Journal of Petrology, 42, 825-845.
1024 Scaillet, B., Holtz, F., and Pichavant, M. (2016) Experimental constraints on the formation of silicic
1025 magmas. Elements, 12, 109-114.
1026 Schaen, A.J., Singer, B.S., Cottle, J.M., Garibaldi, N., Schoene, B., Satkoski, A.M., and Fournelle, J.
1027 (2018) Textural and mineralogical record of low-pressure melt extraction and silicic cumulate
1028 formation in the late Miocene Risco Bayo-Huemul Plutonic Complex, Southern Andes. Journal
1029 of Petrology, 59, 1991–2016.
1030 Sengupta, P., Dasgupta, S., Bhattacharya, P.K., and Mukherjee, M. (1990) An orthopyroxene-biotite
1031 geothermometer and its application in crustal granulites and mantle-derived rocks. Journal of
1032 Metamorphic Geology, 8, 191–197.
1033 Shcherbakov, D., Plechov, P.Y., Izbechov, P.E., and Shipman, J.S. (2011) Plagioclase zoning as an
1034 indicator of magmatic processes at Bezymianny volcano, Kamchatka. Contributions to
1035 Mineralogy and Petrology, 162, 83–99
1036 Shimura, T., Komatsu, M., and Iiyama, J.T. (1992) Genesis of the lower crustal garnet-orthopyroxene
1037 tonalites (S-group) of the Hidaka Metamorphic Belt, northern Japan. Transactions of the Royal
1038 Society of Edinburgh: Earth Sciences, 83, 259–268.
1039 Shimura, T., Owada, M., Osanai, Y., Komatsu, M., and Kagami, H. (2004) Variety and genesis of the
1040 pyroxene-bearing S- and I-type granitoids from the Hidaka metamorphic belt, Hokkaido,
1041 northern Japan: Transactions of the Royal Society of Edinburgh: Earth Sciences, 95, 161–179.
1042 Skjerlie, K.P., and Johnston, A.D. (1993) Fluid-absent melting behavior of an F-rich tonalitic gneiss
1043 at mid-crustal pressures: implications for the generation of anorogenic granites. Journal of
1044 Petrology, 34, 785–815.

Smith, H.A., and Giletti, B.J. (1997) Lead diffusion in monazite. Geochimica et Cosmochimica Acta, 61, 1047–1055.

Spear, F.S. (2014) The duration of near-peak metamorphism from diffusion modelling of garnet zoning. Journal of Metamorphic Geology, 32 (8), 903–914.

Tamic, N., Behrens, H., and Holtz, F. (2001) The solubility of H_2O and CO_2 in rhyolitic melts in equilibrium with a mixed CO_2-H_2O fluid phase. Chemical Geology, 174, 333–347.

Tang, L., Santosh, M., Tsunogae, T., Koizumi, T., Hu, X.K., and Teng, X.M. (2017) Petrology, Phase Equilibria Modelling and Zircon U-Pb Geochronology of Paleoproterozoic Mafic Granulites from the Fuping Complex. Journal of Metamorphic Geology, 35, 517-540.

Tuttle, O.F., and Bowen, N.L. (1958) Origin of granite in the light of experimental studies in the system $NaAlSi_3O_8$-$KAlSi_3O_8$-SiO_2-H_2O. Geological Society of America Memoir, 74, 1–146.

Vernon R. H. (1968) Microstructures of high-grade metamorphic rocks at Broken Hill, Australia. Journal of Petrology, 9, 1–22.

Vernon RH. (1999) Quartz and feldspar microstructures in metamorphic rocks. The Canadian Mineralogist, 37, 513–524.

Vernon R. H. (2004) A practical guide to rock microstructure, Cambridge University Press, Cambridge.

Vernon RH., and Paterson SR. (2008) How extensive are sub-solidus grain-shape changes in cooling granites? Lithos, 105, 42–50.

Vernon RH. (2010) Granites really are magmatic: using microstructural evidence to refute some obstinate hypotheses. (Forster MA, Fitz Gerald JD, Lister GS (eds) The Science of Microstructure). Journal of the Virtual Explorer. 35, 1-36

Vernon R. H., and Collins W. J. (2011) Structural criteria for identifying granitic cumulates. Journal of Geology, 119, 127–142.

Viete, D.R., and Lister, G.S., (2017) On the significance of short-duration regional metamorphism.

Journal of Geology Society, London, 174, 377-392.

Wan, Y.S., Liu, D.Y., Wilde, S.A., Cao, J.J., Chen, B., Dong, C.Y., Song, B., and Du, L.L. (2010) Evolution of the Yunkai Terrane, South China: evidence from SHRIMP zircon U–Pb dating, geochemistry and Nd isotope. Journal of Asian Earth Sciences, 37, 140–153.

Wang, Y.J., Fan, W.M., Zhao, G.C., Ji, S.C., and Peng, T.P. (2007) Zircon U–Pb geochronology of gneisses in Yunkai Mountains and its implications on the Caledonian event in South China. Gondwana Research, 12, 404–416.

Wang, Y.J., Zhang, A.M., Fan, W.M., Zhao, G.C., Zhang, G.W., Zhang, Y.Z., Zhang, F.F., Li, S.Z. (2011) Kwangsian crustal anatexis within the eastern South China Block: Geochemical, zircon U–Pb geochronological and Hf isotopic fingerprints from the gneissoid granites of Wugong and Wuyi–Yunkai Domains. Lithos, 127, 239–260.

Wang, Y.J., and Wu, C.M. (2012) Kwangsian and Indosinian reworking of the eastern South China Block: Constraints on zircon U–Pb geochronology and metamorphism of amphibolites and granulites. Lithos, 150, 227–242.

Wang, Y.J., Zhang, A.M., Fan, W.M., Zhang, Y.H., and Zhang, Y.Z. (2013a). Origin of paleosubduction -modified mantle for Silurian gabbro in the Cathaysia Block: geochronological and geochemical evidence. Lithos, 160–161, 37–54.

Wang, Y.J., Fan, W.M., Zhang, G., and Zhang, Y. (2013b) Phanerozoic tectonics of the South China Block: key observations and controversies. Gondwana Research, 23, 1273–1305.

Wang, D., Zheng. J., Ma, Q., Griffin, W.L., Zhao, H., and Wong, J. (2013c) Early Paleozoic crustal anatexis in the intraplate Wuyi–Yunkai orogen, South China. Lithos, 175–176, 124–145.

Wang, L.J., Guo, J.H., Yin, C.Q., Peng, P., Zhang, J., Spencer, C.J., and Qian, J.H. (2018) High-temperature S-type granitoids (charnockites) in the Jining complex, North China Craton: Restite entrainment and hybridization with mafic magma. Lithos, 320–321, 435–453.

Wen, S., and Nekvasil, H. (1994) SOLVALC: An interactive graphics program package for

calculating the ternary feldspar solvus and for two-feldspar geothermometry. Computer & Geoscience, 20, 1025–1040.

Whitney, D.L., and Evans, B.W. (2010) Abbreviations for names of rock-forming minerals. American Mineralogist, 95 (1): 185–187.

White, A.J.R., and B.W. Chappell. (1977) Ultra-metamorphism and granitoid genesis, Tectonophysics, 43, 185–187.

Wu, C.M., Pan, Y.S., and Wang, K.Y. (1999) Refinement of the biotite-orthopyroxene geothermometer with applications. Acta Petrologica Sinica, 15 (3), 463-468 (in Chinese with English abstract).

Wyborn, D., Chappell, W.B., and Johnston, R.M. (1981) Three S-Type Volcanic Suites From the Lachlan Fold Belt, Southeast Australia. Journal of Geophysical Research, 86 (B11), 10335-10348.

Xia, Q.X., and Zhou, L.G. (2017) Different origins of garnet in high pressure to ultrahigh-pressure metamorphic rocks. Journal of Asian Earth Sciences, 145, 130–148.

Xia, Y., Xu, X.S., Zou, H.B., and Liu, L. (2014) Early Paleozoic crust–mantle interaction and lithosphere delamination in South China Block: evidence from geochronology, geochemistry, and Sr–Nd–Hf isotopes of granites. Lithos, 184–187, 416–435.

Xu, W.J., and Xu, X.S. (2015) Early Paleozoic intracontinental felsic magmatism in the South China Block: petrogenesis and geodynamics. Lithos, 234–235, 79–92.

Yao, W.H., Li, Z.X., Li, W.X., Wang, X.C., Li, X.H., and Yang, J.H. (2012) Post-kinematic lithospheric delamination of the Wuyi–Yunkai orogen in South China: evidence from ca. 435 Ma high-Mg basalts. Lithos, 154, 115–129.

Yang, Q.Y., Santosh, M., and Tsunogae, T. (2014) First report of Paleoproterozoic incipient charnockite from the North China Craton: implications for ultrahigh temperature metasomatism. Precambrian Research, 243, 168–180.

Yu, J.H., Zhou, X.M., and Zhao, L. (2003) Discovery and implications of granulite facies metamorphic rocks in the eastern Nanling, China. Acta Petrologica Sinica, 19 (3), 461–467 (in Chinese with English abstract).

Yu, J.H., Zhou, X.M., and O'Reilly, S.Y. (2005) Formation history and protolith characteristics of granulite facies metamorphic rock in Central Cathaysia deduced from U–Pb and Lu–Hf isotopic studies of single zircon grains. Chinese Science Bulletin, 50 (18), 2080–2089.

Yu, J.H., Wang, L.J., Wei, Z.Y., Sun, T., and Shu, L.S. (2007) Phanerozoic metamorphic episodes and characteristics of Cathaysia Block. Geological Journal of China Universities, 13 (3), 474–483 (in Chinese with English abstract).

Yu J H, Lou F S., and Wang L J. (2014) The geological significance of a Paleozoic mafic granulite found in the Yiyang area of northeastern Jiangxi Province (in Chinese). Chinese Science Bulletin (Chinese Version), 59, 3508–3516.

Yu, X., and Lee, C.T.A. (2016) Critical porosity of melt segregation during crustal melting: constraints from zonation of peritectic garnets in a dacite volcano. Earth and Planetary Science Letters, 449, 127–134.

Yu, Y., Huang, X.L., Sun, M., and He, P.L. (2018) Petrogenesis of granitoids and associated xenoliths in the early Paleozoic Baoxu and Enping plutons, South China: Implications for the evolution of the Wuyi-Yunkai intracontinental orogen. Journal of Asian Earth Science, 156, 59–74.

Zhao, K., Xu, X.S., and Erdmann, S. (2017) Crystallization conditions of peraluminous charnockites: constraints from mineral thermometry and thermodynamic modeling. Contribution to Mineralogy and Petrology, 172, 26.

Zhao, K., Xu, X.S., and Erdmann, S. (2018) Thermodynamic modeling for an incrementally fractionated granite magma system: Implications for the origin of igneous charnockite. Earth and Planetary. Science Letters, 499, 230-242.

Zhao, L., Zhou, X.W., Zhai, M.G., Santosh, M., Ma, X.D., Shan, H.X., and Cui, X.H. (2014).

Paleoproterozoic tectonic transition from collision to extension in the eastern Cathaysia Block, South China: evidence from geochemistry, zircon U–Pb geochronology and Nd–Hf isotopes of a granite–charnockite suite in southwestern Zhejiang. Lithos, 184–187, 259–280.

Zhang, Q., Jiang, Y.-H., Wang, G. C., Liu, Z., Ni, C. Y., and Qing, L. (2015) Origin of Silurian gabbros and I-type granites in central Fujian, SE China: implications for the evolution of the early Paleozoic orogen of South China. Lithos, 216–217, 285–297.

Zhang, S.H., Zhao, Y., and Song, B. (2006) Hornblende thermobarometry of the Carboniferous granitoids from the Inner Mongolia Paleouplift: implications for the tectonic evolution of the northern margin of North China block. Mineral and Petrology, 87, 123–141.

Figure captions

Figure 1. (a) Tectonic schematic map of the South China Block; **(b)** Geologic map of the Gaozhou Complex in Yunkai terrane (modified after Chen et al. (2012), Wang et al. (2013)) and the sampling locations of the Yunlu garnet-bearing charnockite.

Figure 2. Representative outcrops and photomicrographs of the Yunlu charnockite. **(a)** Garnet-bearing charnockite and Grt-Bt gneiss xenolith. **(b)** Xenolith is mainly composed of Bt, Grt, Pl and Qz. **(c)-(f)** Micro-textures of the charnockite. **(c)** Euhedral orthopyroxene crystals are replaced by biotite + quartz intergrowth. **(d)** symplectite texture composed of quartz + garnet on boundaries between orthopyroxene and plagioclase. **(e)**, garnet crystals forming a cluster, or glomerocryst, in charnockite, while part of garnet grain is replaced by biotite + quartz intergrowth. **(f)** Euhedral to subhedral, tabular plagioclase crystals are impinged to form a skeleton texture, which is filled by anhedral, interstitial quartz crystals.

Figure 3. Backscattered electron images of the symplectite textures on Yunlu charnockite. **(a)** Symplectite of quartz (Qz_3) + garnet (Grt_3) on boundaries between orthopyroxene and plagioclase. **(b)** Symplectite of quartz (Qz_3) + K-feldspar (Kfs_2) + garnet (Grt_3) on boundaries between biotite and plagioclase. **(c)-(d)** Symplectite of quartz (Qz_3) + garnet (Grt_3) on

boundaries between ilmenite and plagioclase.

Figure 4. (a) Backscattered electron image of group1 (Grt_1) euhedral garnet. **(b)** Y element compositional profile across the garnet crystal in figure **(a)**. **(c)** Compositional profile of almandine, pyrope, grossular and spessartine contents of the garnet crystal from the figure **(a)**. **(d)** REE compositions of group 1, group 2 (Grt_2) and group 3 (Grt_3) garnets. The grey pattern represents the garnet REE contents from peraluminous granites (data from Rong et al. (2018), see Appendix Table 8). **(e)** The plot of CaO versus MnO for group 1 and group 2 garnets (modified from Narduzzi et al., 2017). Garnets from Bt-Grt gneiss xenolith is compared. **(f)** Plot of CaO versus MgO contents for group 1, group 2 garnets and group 3 garnets, respectively.

Figure 5. (a) X_{Mg} vs. X_{Al} diagram for orthopyroxene compositions. The data of magmatic Opx from igneous charnockite are from Clemens and Birch (2012); Clemens and Phillips (2014); Shimura et al. (1992); and Wyborn (1981). The data of metamorphic Opx from incipient charnockite are from Rajesh et al. (2011); Hansen et al. (1987); Santosh et al. (1990). The data of peritectic Opx from melting experiments and granulites are from Montel and Vielzuef (1997); Patino Douce and Beard (1996); Nair and Chacko (2002); Berman and Bostock (1997); Dempster et al. (1991); Harley et al. (1990); Baba (1999) and Harley (1998). **(b)** REE compositions of Opx_1 from Yunlu charnockite, peritectic orthopyroxenes from psammitic granulites (Lavaure and Sawyer 2011) are also plotted for comparison. **(c)** Diagrams of $Mg^{\#}$ of Opx_1, Opx_2 and Grt_1, Grt_2 crystals, the grey dot represents the garnet and orthopyroxene compositions from melting experiments results where the starting materials are felsic metapelites, gneisses and granites (SiO_2 = 65-75 wt%, data from Carrington and Harley (1995); Conrad et al. (1988); Montel and Vielzeuf (1997); Skjerlie and Johnston (1993). **(d)** Biotite compositions for the Yunlu charnockite with temperature contours from Henry et al., (2002, 2005). The uncertainty of the temperature estimate is ~60 °C. **(e)** Compositional profile of individual plagioclase crystal from Yunlu charnockite. **(f)** Histogram showing the anorthite contents of plagioclase.

Figure 6. Characteristic Raman spectrum of fluid inclusions in quartz crystals of the Yunlu charnockite with CO_2-H_2O-rich **(a)** and H_2O-rich **(b)** compositions, respectively. Among all 13 analyzed fluid inclusions, only one inclusion shows CO_2-H_2O-rich characteristic, while the rest of twelve fluid inclusions show H_2O-rich characteristics.

Figure 7. T-H_2O in melt diagram of comparison phase relations determined by rhyolite-MELTS modeling and those determined in crystallization experiments reported by Clemens and Birch (2012). The sub-vertical, stippled lines are the calculated isopleths for the concentration of H_2O dissolved in the melt (Newman and Lowenstern 2002). The thickened, dotted curves are the phase boundaries determined by Clemens and Birch (2012), while the thickened, solid curves are the modeled phase boundaries for various initial H_2O contents (2.0-7.0 wt%) constrained by rhyolite-MELTS modeling. The modeled phase boundaries of various minerals are made by following steps. We first constrain the equilibrium crystallization processes of initial composition under various initial H_2O contents, while the pressure and oxygen fugacity remain constant. We then plot the crystallization path (fitted by saturated points of various minerals) according to the temperatures and H_2O contents in melts for each crystallizing mineral. Finally, the phase-saturated points of same minerals for various initial H_2O contents are fitted to yield a curve, which is the mineral saturated boundary shown by thickened, solid curves. The phase-saturated boundaries of other minerals are also made by this method.

Fig. 8. (a–f) Harker diagrams showing the major element compositions of the Yunlu charnockite (blue circle) and the modeled compositional evolution for incremental fractionation (lines with different colors). D19-4 is the most felsic charnockite in Yunlu pluton, while MC01 is the synthetic composition which consist of 60% charnockite 15GZ19 and 40% interstitial melt (Table 3; Appendix Table 5). Please refer to the supplementary material for detailed descriptions. The green area represents the compositions of experimental melt derived from meta-sedimentary rocks (Appendix Table 4).

Fig. 9. (a) Rhyolite-MELTS modeling results of H_2O-CO_2 evolution paths during magma crystallization at different initial H_2O + CO_2 contents. The filled- and open-symbols on lines with different color represent CO_2 and H_2O evolutional curve, respectively. All the modeling results shown above are presented in Appendix Table 6. The solidus temperature is calculated by the methods from Papale et al. (2006) and Newman and Lowenstern (2002).

Figure 10. (a)-(d) Rhyolite-MELTS modeling results of mineral crystallization sequences and water concentration in the residual melts of the sample MC01 (Gualda et al. 2012; Gualda and Ghiorso 2015) assuming initial H_2O contents of 2.0-5.0 wt%. The H_2O-saturated content is restricted to 10.0 wt% according to Tamic et al. (2001) and Holtz et al. (2001).

Fig. 11. **(a)** Model diffusion profiles of a grossular content in Grt_1 at various timescales at given diffusion coefficients compared with measured profile in garnet rim. **(b)** Diffusion length (m) as a function of time (year), blue solid line is contoured for diffusion coefficient. The given inter-diffusion coefficients of various element in minerals are shown in Table S1 in supplementary material.

Figure 12. Crystallization sequences of different minerals along with the decrease of temperature (from liquidus to solidus) of sample MC01, given by rhyolite-MELTS modeling (4.0 wt% initial H_2O content). The mineral-saturated temperatures are constrained by modeling results of the rhyolite-MELTS coupled with experimental data from Clemens and Birch (2012). The temperature results yielded by various thermometers are marked in plot and the speculative melt extraction window is shown. Please see text for further discussion.

This is the peer-reviewed, final accepted version for American Mineralogist, published by the Mineralogical Society of America.
The published version is subject to change. Cite as Authors (Year) Title. American Mineralogist, in press.
DOI: https://doi.org/10.2138/am-2020-7335. http://www.minsocam.org/

1242 Table 1. Mineral shape, size, inclusion, occurrence and compositions from Yunlu garnet-bearing charnockite.

Mineral	Type	Shape	Size (mm)	Mineral inclusion	Occurrence/ distribution	Average composition	Reference figure
Orthopyroxene	Opx_1	euhedral	0.5-6	quartz, plagioclase, biotite	# enclosed by Bt_2+Qz_2	X_{Fs} = 53.6; X_{En} = 45.9	Fig. 2d
	Opx_2	subhedral to anhedral					Fig. 2c
Garnet	Grt_1	euhedral	1-6	quartz, ilmenite	# enclosed by Bt_2+Qz_2	X_{Alm} = 67; X_{Prp} = 25 X_{Grs} = 4.7; X_{Sps} = 3.1	Fig. 2e
	Grt_2	subhedral to anhedral	1-3				
	Grt_3	anhedral	0.01-0.1	none	coexistence with Qz_3	X_{Alm} = 70; X_{Pyp} = 20 X_{Grs} = 6.1; X_{Sps} = 4.1	Fig. 3
Biotite	Bt_1	euhedral	0.4-5	none	# coexistence with Qz_2	X_{Fe} = 0.46; X_{Mg} = 0.40; X_{Ti} = 0.10; X_{Al} = 0.04	Fig. 2d
	Bt_2	subhedral to anhedral	0.5-2	quartz			Fig. 2c
Plagioclase	Pl_1	euhedral to subhedral	0.5-3	none	#	X_{An} = 0.44, X_{Ab} = 0.53	Fig. 2f
	Pl_2					X_{An} = 0.35, X_{Ab} = 0.61	Fig. 3
K-feldspar	Kfs_1	subhedral to anhedral	0.5-30	none	# coexistence with Qz_3,	X_{Or} = 0.85, X_{Ab} = 0.14	Fig. 2f
	Kfs_2	anhedral	0.01-0.03	none		X_{Or} = 0.92, X_{Ab} = 0.07	Fig. 3b
Quartz	Qz_1	euhedral to subhedral	0.5-4	none	# coexistence with Bt_2	--	Fig. 2d
	Qz_2	anhedral	0.2-0.5	none			Fig. 2c
	Qz_3	anhedral	0.02-0.05	none	coexistence with Grt_3		Fig. 3

1243 Notes: The "#" means that the $Opx_{1, 2}$, $Grt_{1, 2}$, Bt_1, Pl_1, $Kfs_{1,}$ and Qz_1 are coexistent mineral assemblages. The Pl_1
1244 represents the continuous core-rim composition with normal An zoning in plagioclase crystal. The Pl_2 represents the
1245 plagioclase composition that is adjacent to the Grt_3 crystals, which has lowest An content.
1246
1247

This is the peer-reviewed, final accepted version for American Mineralogist, published by the Mineralogical Society of America.
The published version is subject to change. Cite as Authors (Year) Title. American Mineralogist, in press.
DOI: https://doi.org/10.2138/am-2020-7335. http://www.minsocam.org/

1248 Table 2. Temperature and pressure results of the Yunlu garnet-bearing charnockite.

Stage	Method	Temperature (°C)						Pressure (MPa)
		Grt-Opx thermometry	Grt-Bt thermometry	Bt-Opx thermometry	Two-feldspar thermometry			Grt-Opx-Pl-Qz Barometry
					Ghiorso (1984)	F&L (1988)	E&G (1990)	
Magmatic crystallization	Mineral pair	$Grt_{1,2}$ - $Opx_{1,2}$	$Grt_{1,2}$ - Bt_1	Bt_1 - $Opx_{1,2}$	Pl_1 rim - Kfs_1 core			$Grt_{1,2}$ - $Opx_{1,2}$ - Pl_1 -Qz_1
	Results	820	770	780	642	623	630	610
Metamorphic overprint	Mineral pairs	Grt_3 - $Opx_{1,2}$ rim	Grt_3 - $Bt_{1,2}$ rim	--		--		Grt_3 - $Opx_{1,2}$ rim - Pl_2 - Qz_3
	Results	750	720					710

1249 Notes: Grt-Opx thermometry and Grt-Opx-Pl-Qz barometry: Bhattacharya et al. (1991); Grt-Bt thermometry: Holdaway (2000);
1250 Opx-Bt thermometry: Wu et al. (1999); F&L (1988): Fuhrman and Lindsley (1988); E&G (1990): Elkins and Grove (1990). Note that
1251 in order to avoid the diffusion re-equilibrium result from cooling and later metamorphic overprint, only the core and mantle
1252 compositions of the $Grt_{1,2}$, $Opx_{1,2}$ and Bt_1 crystals with grain size ≥ 4 mm are chosen for thermometric calculations. In addition,
1253 considering the K-Na inter-diffusion in K-feldspar, only the big Kfs_1 core compositions with grain size ≥ 10 mm are used for
1254 thermometric calculation
1255

This is the peer-reviewed, final accepted version for American Mineralogist, published by the Mineralogical Society of America.
The published version is subject to change. Cite as Authors (Year) Title. American Mineralogist, in press.
DOI: https://doi.org/10.2138/am-2020-7335. http://www.minsocam.org/

Table 3. Starting materials used for thermodynamic modeling. The sample LMI 9399 is cited from Clemens and Birch (2012), while sample D19-4 is cited from Wang et al. (2013). The virtual sample MC01 is composed of 60 % most mafic charnockite 15GZ19 plus 40% minimum melt composition, please see section 5.1.2 for detailed description.

Sample	SiO_2	TiO_2	Al_2O_3	FeO^*	MnO	MgO	CaO	Na_2O	K_2O	ASI	$Mg^\#$
LMI 9399	69.83	0.65	14.75	4.21	0.05	1.50	2.76	2.45	3.79	1.11	38.9
D19-4	68.65	0.76	14.36	4.88	0.10	1.86	3.92	2.43	1.63	1.12	40.7
MC01	68.16	0.85	14.14	4.94	0.07	1.59	2.67	2.74	3.20	1.10	36.7

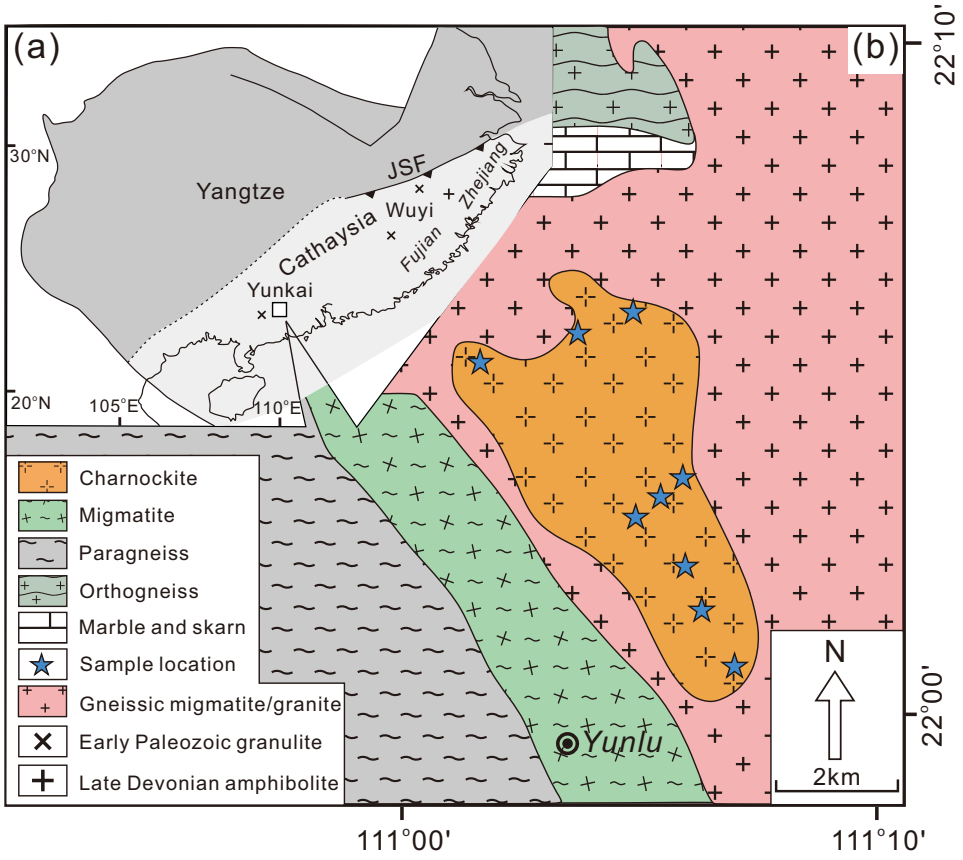
(a)
(b)
30°N
20°N
105°E
110°E
Yangtze
JSF
Cathaysia
Wuyi
Zhejiang
Fujian
Yunkai
Charnockite
Migmatite
Paragneiss
Orthogneiss
Marble and skarn
Sample location
Gneissic migmatite/granite
Early Paleozoic granulite
Late Devonian amphibolite
Yunlu
N
2km
22°10'
22°00'
111°00'
111°10'

Fig. 1

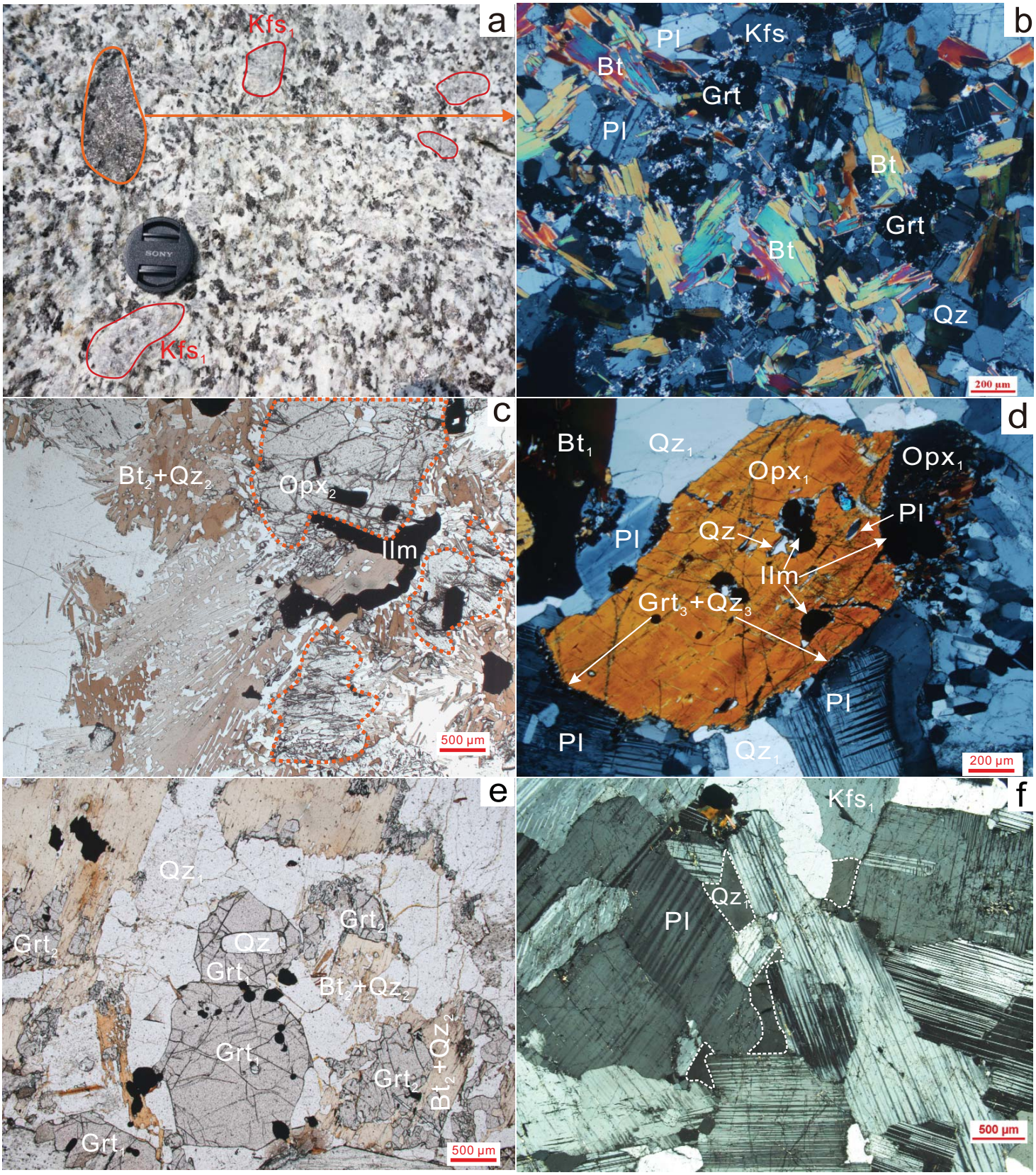
a
Kfs1
Kfs1
b
Pl
Kfs
Bt
Grt
Pl
Bt
Grt
Bt
Qz
200 μm
c
Bt2+Qz2
Opx2
Ilm
500 μm
d
Bt1
Qz1
Opx1
Opx1
Pl
Pl
Qz
Ilm
Grt3+Qz3
Pl
Pl
Qz1
200 μm
e
Qz1
Grt2
Grt2
Qz
Grt1
Bt2+Qz2
Grt1
Grt2
Bt2+Qz2
Grt1
500 μm
f
Kfs1
Qz1
Pl
500 μm

Fig. 2

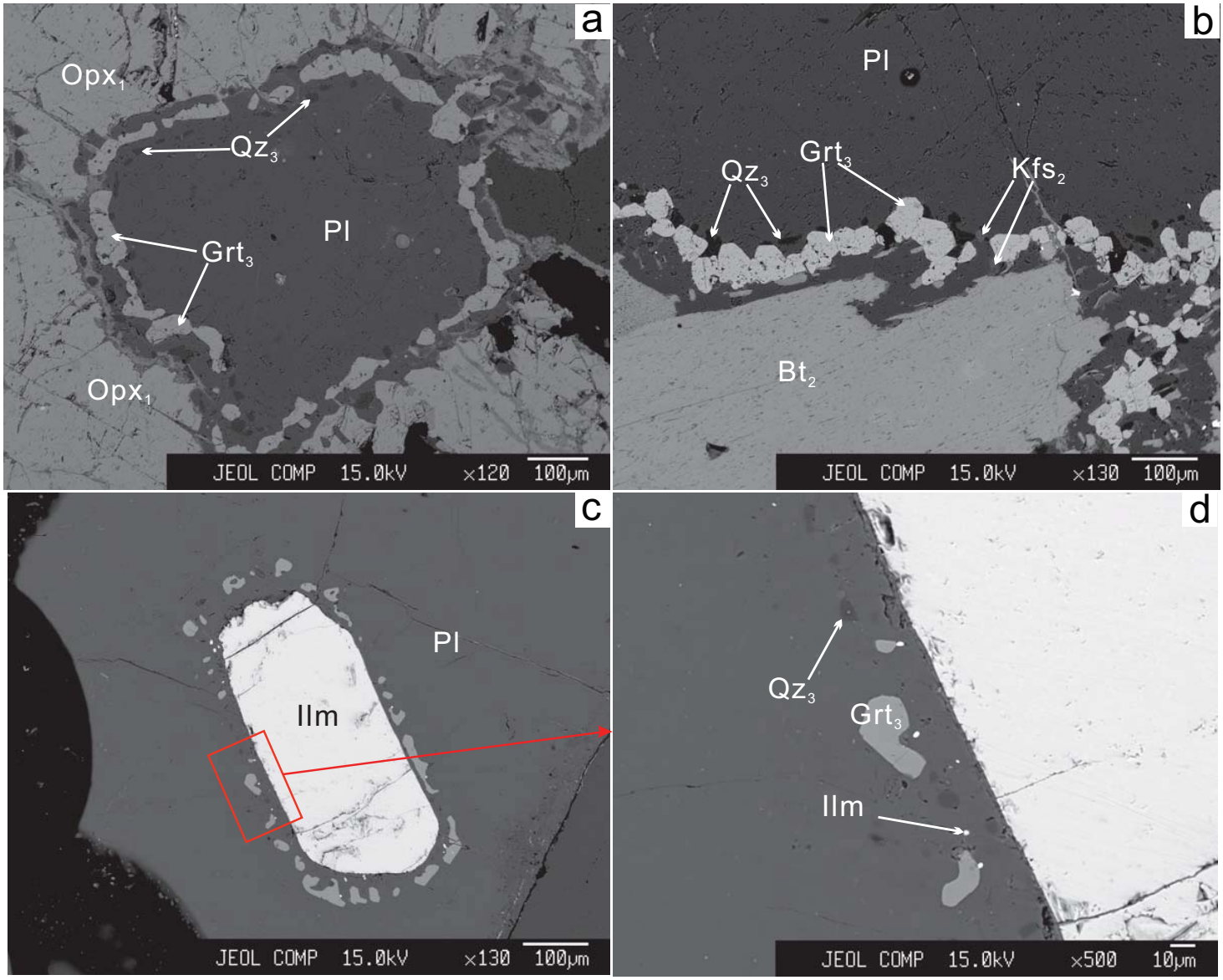
a
Opx1
Qz3
Pl
Grt3
Opx1
JEOL COMP 15.0kV ×120 100μm
b
Pl
Qz3
Grt3
Kfs2
Bt2
JEOL COMP 15.0kV ×130 100μm
c
Pl
Ilm
JEOL COMP 15.0kV ×130 100μm
d
Qz3
Grt3
Ilm
JEOL COMP 15.0kV ×500 10μm

Fig. 3

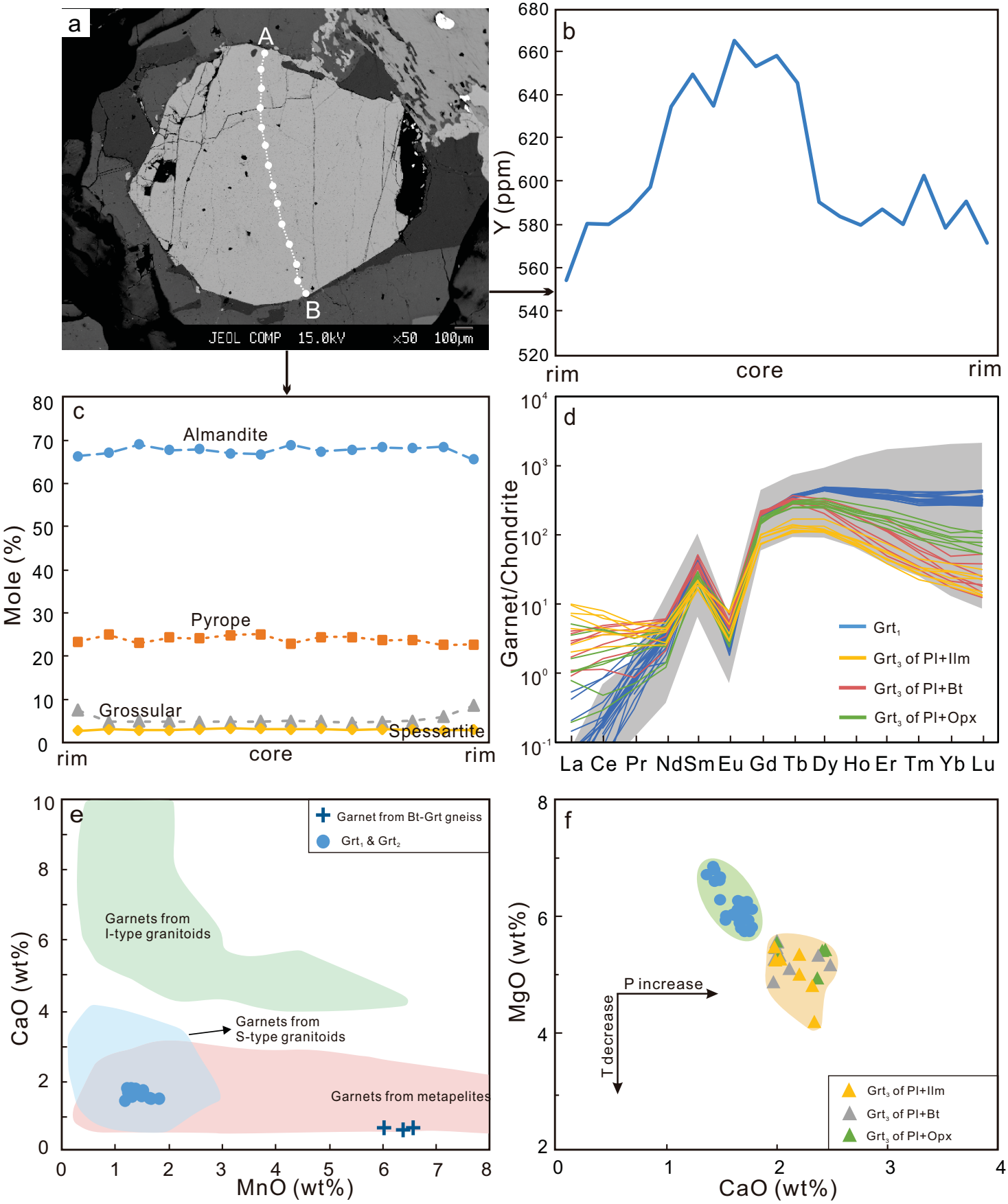
a
A
B
JEOL COMP 15.0kV ×50 100μm
b
Y (ppm)
680
660
640
620
600
580
560
540
520
rim
core
rim
c
Almandite
Pyrope
Grossular
Spessartite
Mole (%)
80
70
60
50
40
30
20
10
0
rim
core
rim
d
Garnet/Chondrite
10^4
10^3
10^2
10^1
10^0
10^{-1}
La Ce Pr Nd Sm Eu Gd Tb Dy Ho Er Tm Yb Lu
Grt$_1$
Grt$_3$ of Pl+Ilm
Grt$_3$ of Pl+Bt
Grt$_3$ of Pl+Opx
e
Garnet from Bt-Grt gneiss
Grt$_1$ & Grt$_2$
Garnets from I-type granitoids
Garnets from S-type granitoids
Garnets from metapelites
CaO (wt%)
MnO (wt%)
f
MgO (wt%)
CaO (wt%)
P increase
T decrease
Grt$_3$ of Pl+Ilm
Grt$_3$ of Pl+Bt
Grt$_3$ of Pl+Opx

Fig. 4

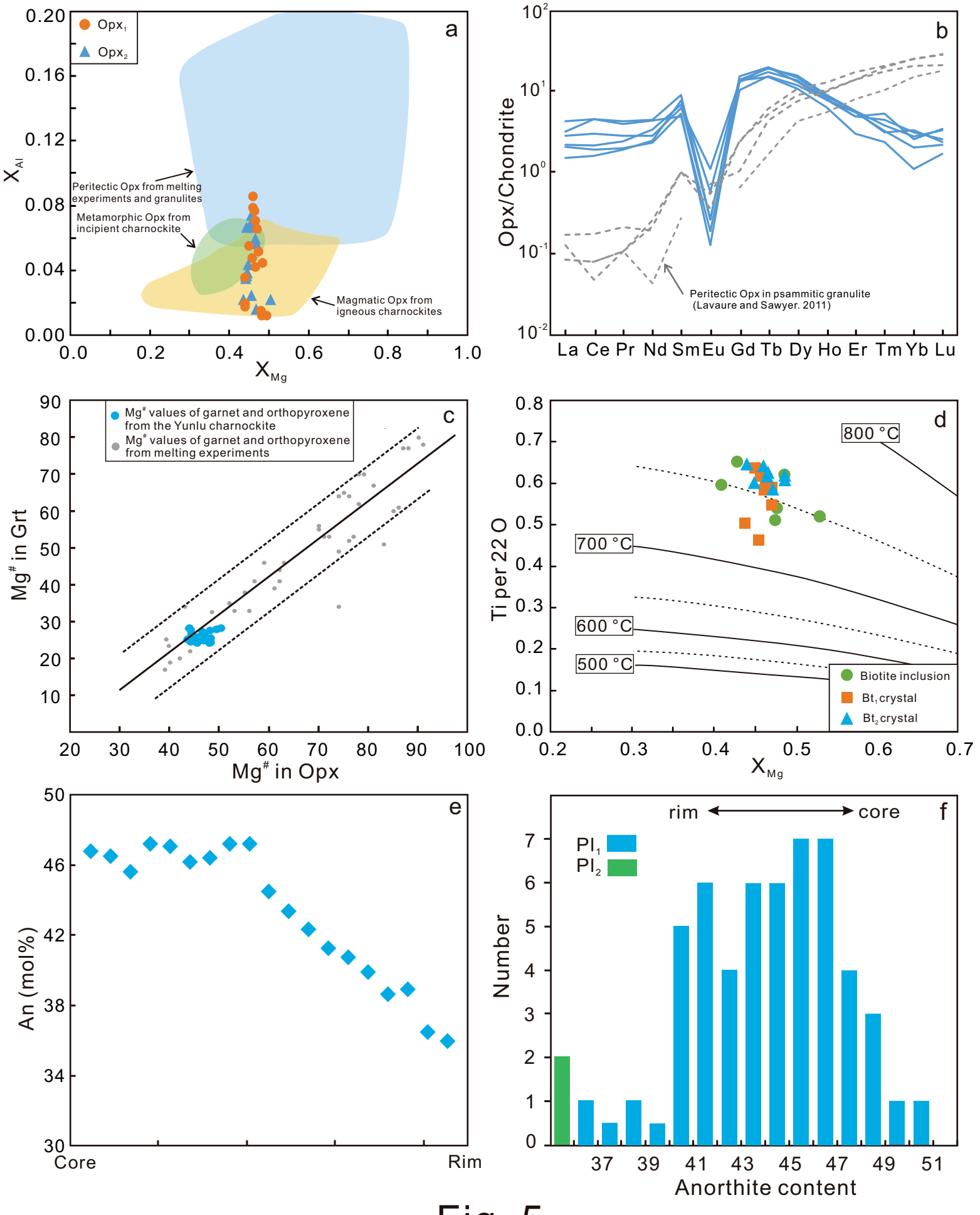
a
Opx1
Opx2
Peritectic Opx from melting experiments and granulites
Metamorphic Opx from incipient charnockite
Magmatic Opx from igneous charnockites
XAl
XMg
b
Opx/Chondrite
Peritectic Opx in psammitic granulite (Lavaure and Sawyer. 2011)
La Ce Pr Nd Sm Eu Gd Tb Dy Ho Er Tm Yb Lu
c
Mg# values of garnet and orthopyroxene from the Yunlu charnockite
Mg# values of garnet and orthopyroxene from melting experiments
Mg# in Grt
Mg# in Opx
d
800 °C
700 °C
600 °C
500 °C
Biotite inclusion
Bt1 crystal
Bt2 crystal
Ti per 22 O
XMg
e
An (mol%)
Core
Rim
f
rim
core
Pl1
Pl2
Number
Anorthite content

Fig. 5

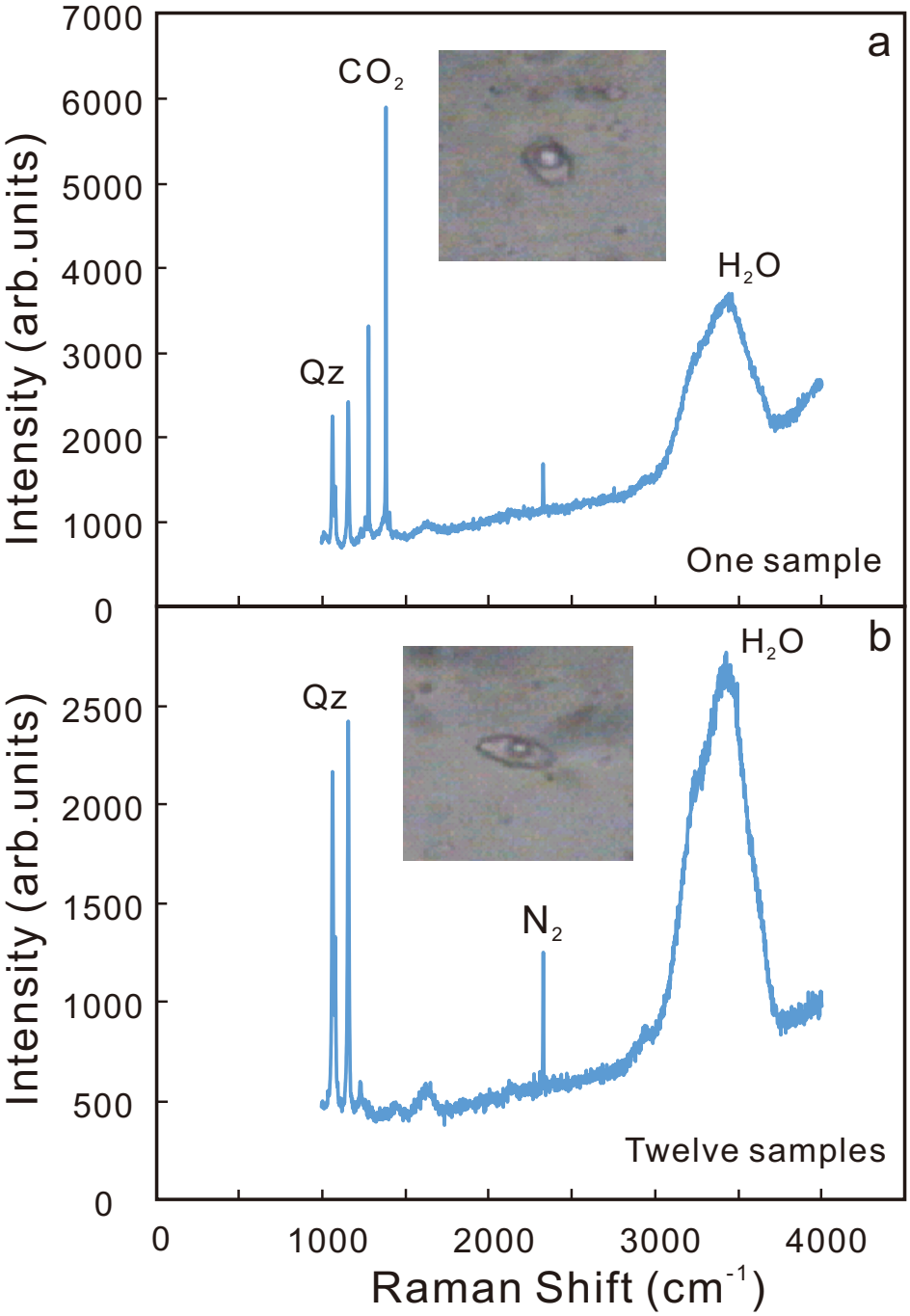
a
b
CO_2
Qz
H_2O
One sample
N_2
Twelve samples
Intensity (arb.units)
Raman Shift (cm^{-1})
0
1000
2000
3000
4000
5000
6000
7000
500
1500
2500

Fig. 6

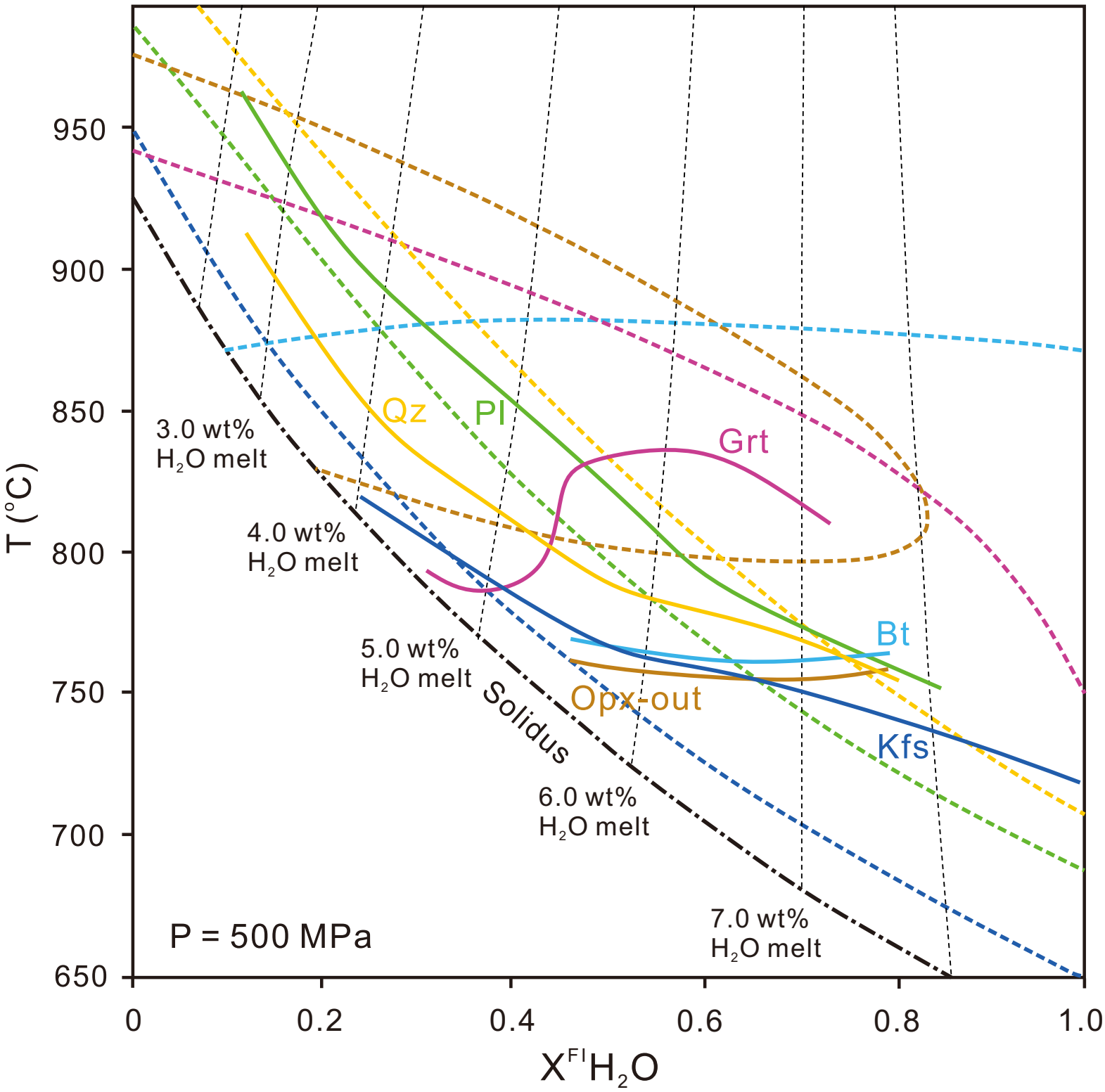
950
900
850
800
750
700
650
T (°C)
0
0.2
0.4
0.6
0.8
1.0
$X^{Fl}H_2O$
3.0 wt%
H_2O melt
4.0 wt%
H_2O melt
5.0 wt%
H_2O melt
6.0 wt%
H_2O melt
7.0 wt%
H_2O melt
Solidus
Qz
Pl
Grt
Bt
Opx-out
Kfs
P = 500 MPa

Fig. 7

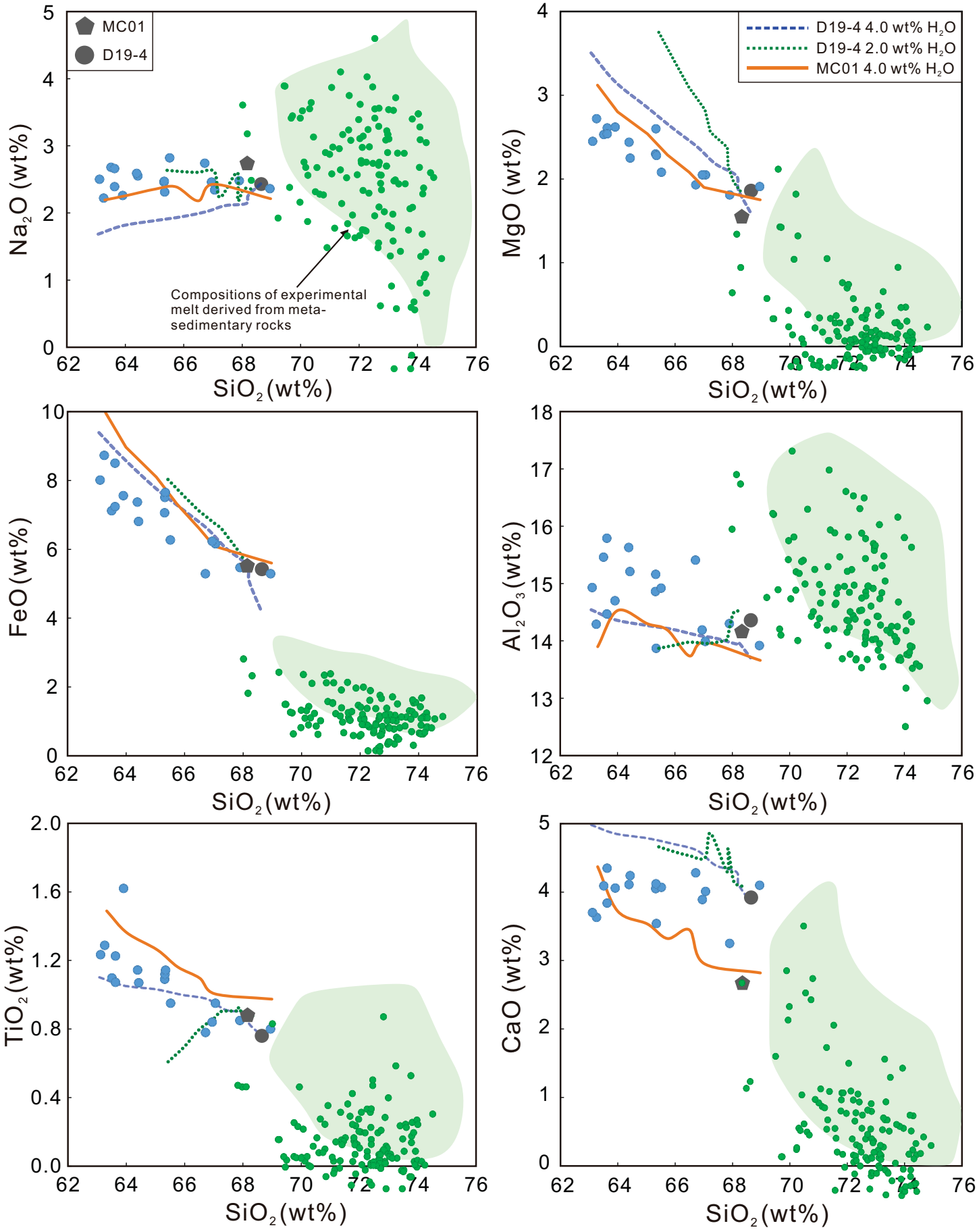
MC01
D19-4
Compositions of experimental melt derived from meta-sedimentary rocks
D19-4 4.0 wt% H2O
D19-4 2.0 wt% H2O
MC01 4.0 wt% H2O
Na2O (wt%)
MgO (wt%)
FeO (wt%)
Al2O3 (wt%)
TiO2 (wt%)
CaO (wt%)
SiO2 (wt%)

Fig. 8

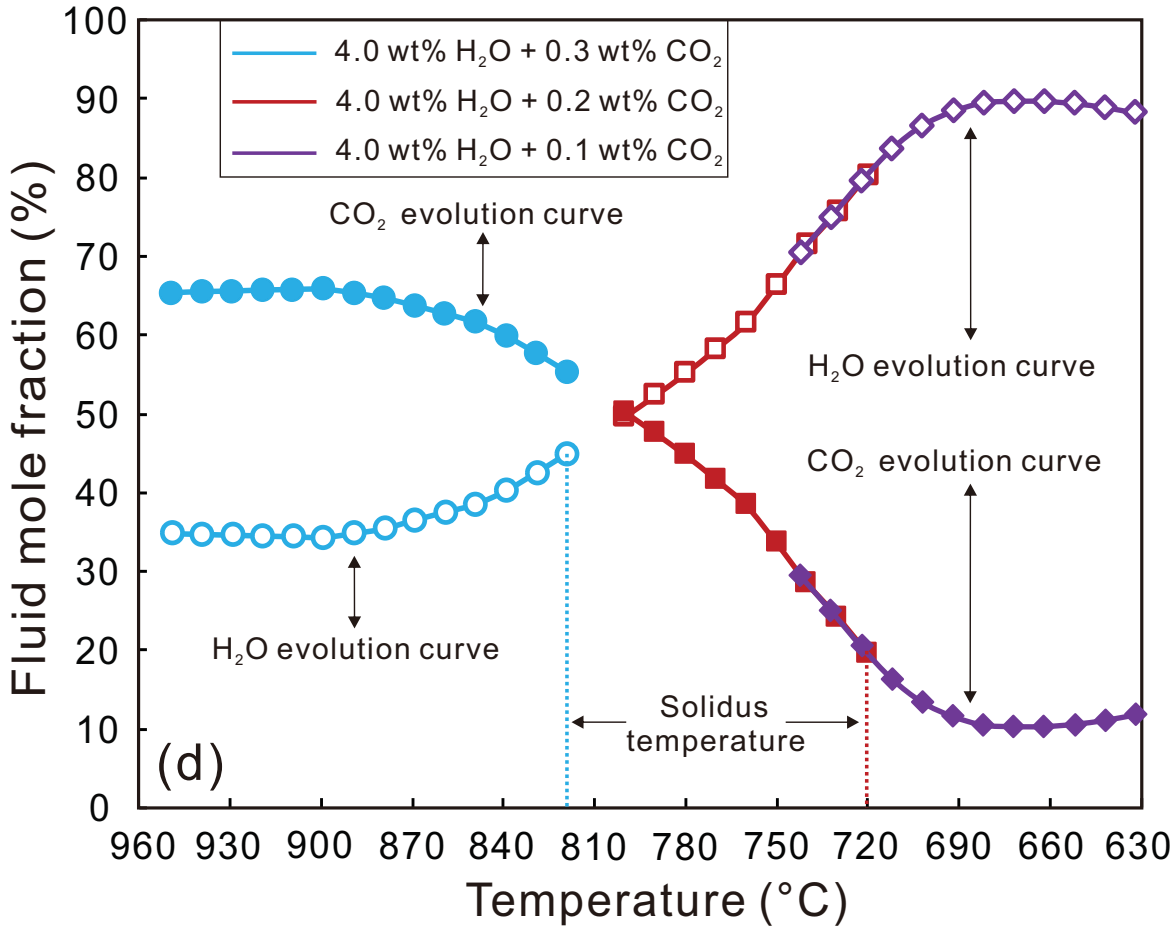
4.0 wt% H2O + 0.3 wt% CO2
4.0 wt% H2O + 0.2 wt% CO2
4.0 wt% H2O + 0.1 wt% CO2
CO2 evolution curve
H2O evolution curve
H2O evolution curve
CO2 evolution curve
Solidus temperature
(d)
Fluid mole fraction (%)
Temperature (°C)
100
90
80
70
60
50
40
30
20
10
0
960 930 900 870 840 810 780 750 720 690 660 630

Fig. 9

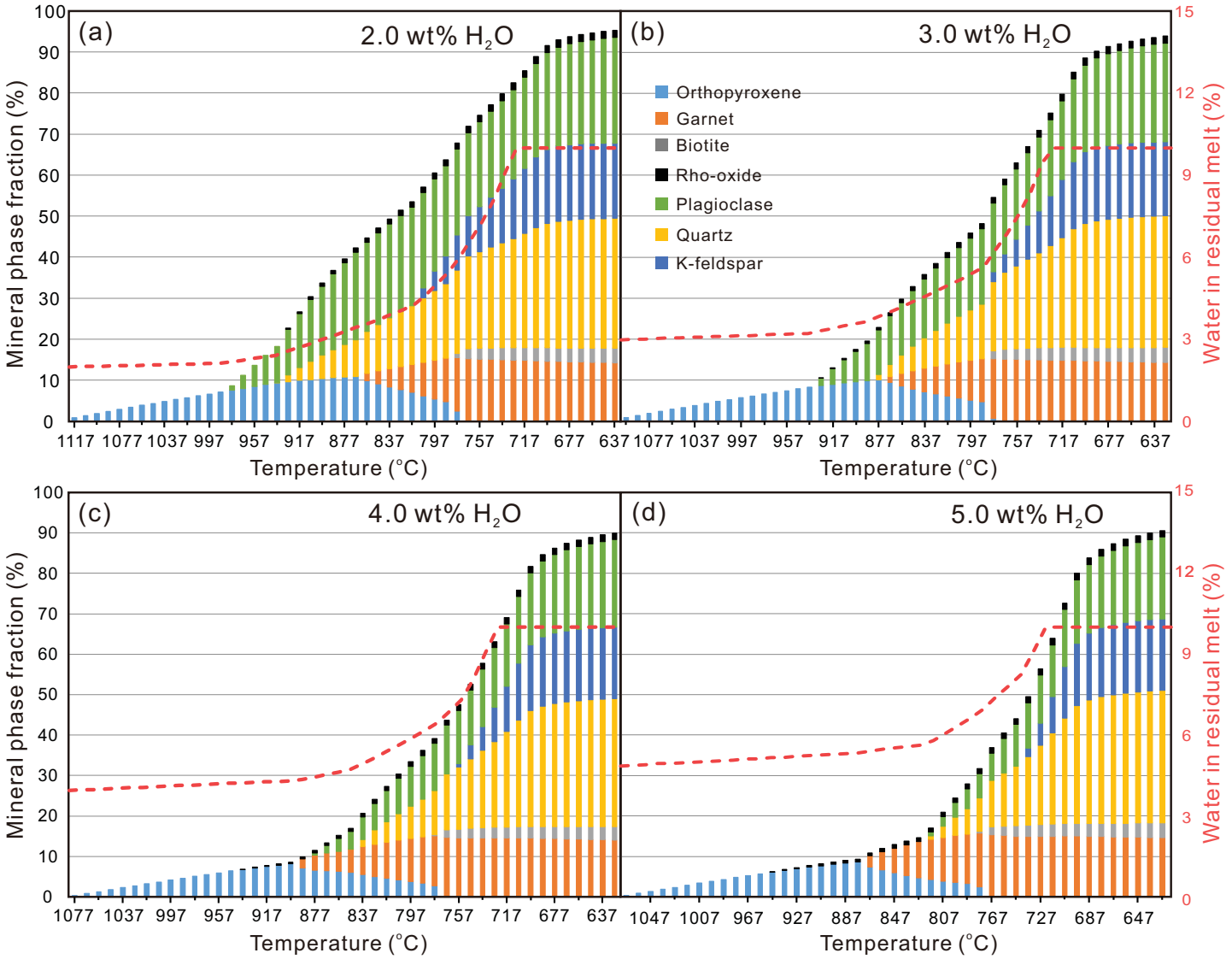
(a)
2.0 wt% H2O
(b)
3.0 wt% H2O
(c)
4.0 wt% H2O
(d)
5.0 wt% H2O
Orthopyroxene
Garnet
Biotite
Rho-oxide
Plagioclase
Quartz
K-feldspar
Mineral phase fraction (%)
Water in residual melt (%)
Temperature (°C)

Fig. 10

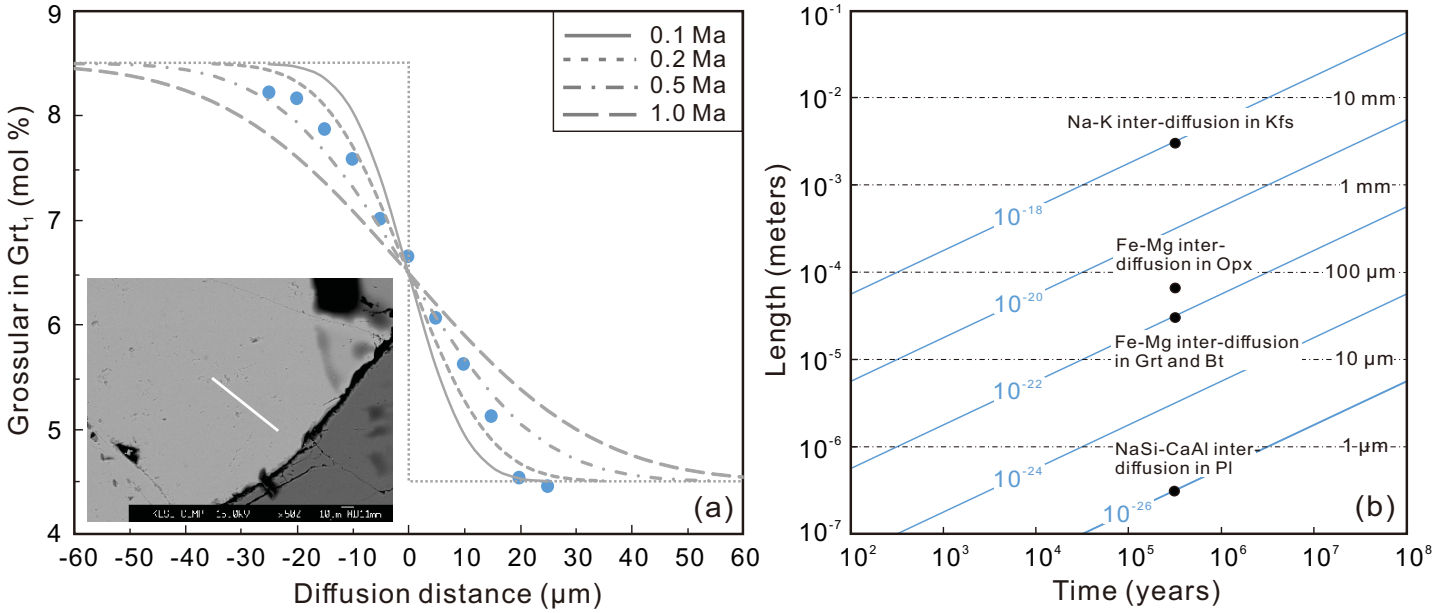
0.1 Ma
0.2 Ma
0.5 Ma
1.0 Ma
Grossular in Grt1 (mol %)
Diffusion distance (μm)
(a)
Length (meters)
Time (years)
Na-K inter-diffusion in Kfs
Fe-Mg inter-diffusion in Opx
Fe-Mg inter-diffusion in Grt and Bt
NaSi-CaAl inter-diffusion in Pl
10 mm
1 mm
100 μm
10 μm
1 μm
(b)

Fig. 11

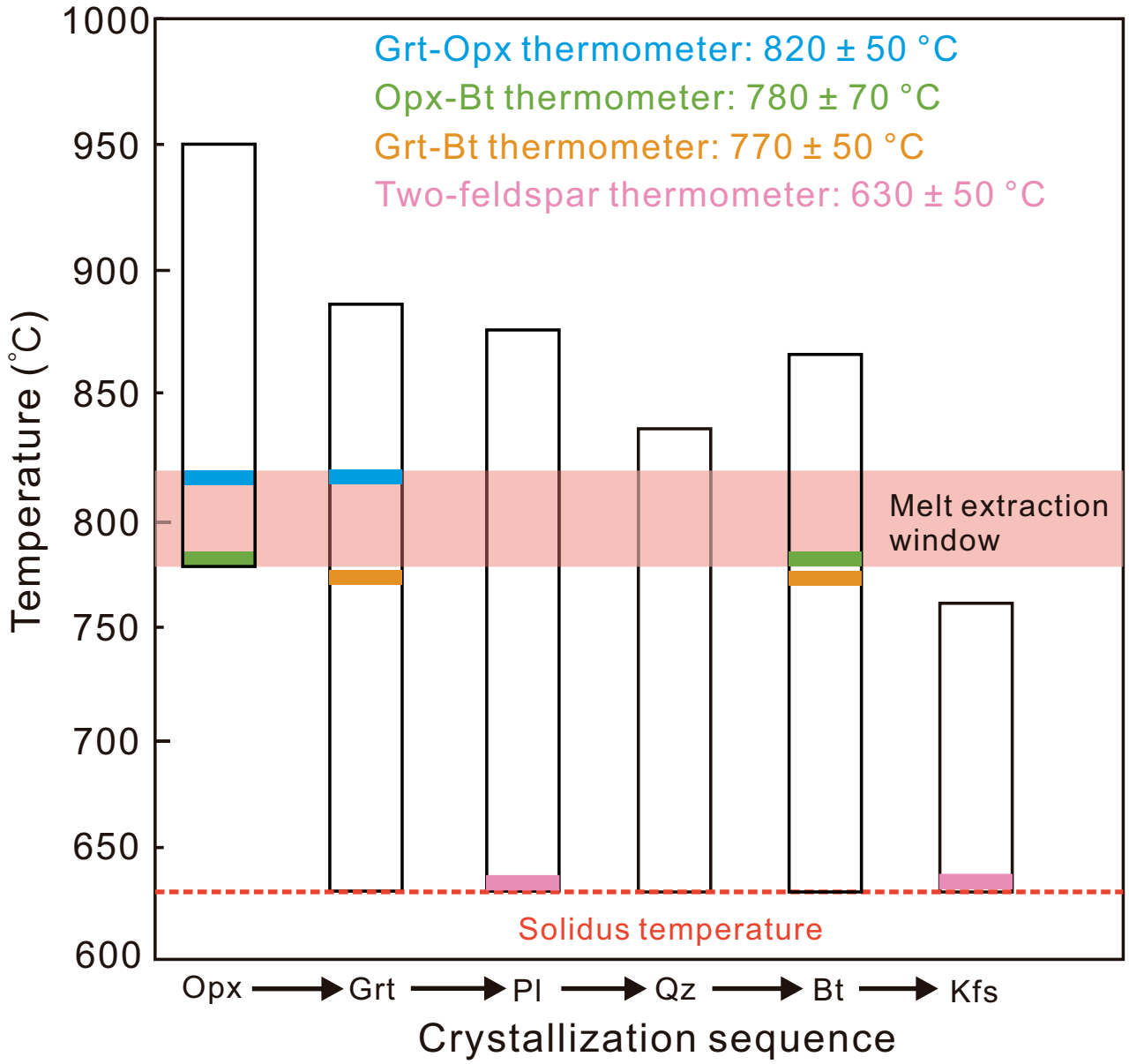
Grt-Opx thermometer: 820 ± 50 °C
Opx-Bt thermometer: 780 ± 70 °C
Grt-Bt thermometer: 770 ± 50 °C
Two-feldspar thermometer: 630 ± 50 °C
Melt extraction window
Solidus temperature
Temperature (°C)
1000
950
900
850
800
750
700
650
600
Opx → Grt → Pl → Qz → Bt → Kfs
Crystallization sequence

Fig. 12